Microscale data to macroscale processes: a review of microcharacterization applied to mineral systems

MARK A. PEARCE[1,2]*, BÉLINDA M. GODEL[1], LOUISE A. FISHER[1], LOUISE E. SCHONEVELD[1,3], JAMES S. CLEVERLEY[1,4], NICHOLAS H. S. OLIVER[5,6] & MICHAEL NUGUS[7]

[1]*CSIRO Mineral Resources, Australian Resources Research Centre, 26 Dick Perry Avenue, Kensington, WA 6151, Australia*

[2]*Department of Applied Geology, Curtin University, GPO Box U1987, Perth, WA 6845, Australia*

[3]*Present address: Research School of Earth Sciences, Australian National University, Canberra, ACT 2601, Australia*

[4]*Present address: Reflex, 216 Balcatta Road, Balcatta, WA 6021, Australia*

[5]*Economic Geology Research Centre, James Cook University, Townsville, QLD 4811, Australia*

[6]*HCOV Global, PO Box 3533, Hermit Park, QLD 4812, Australia*

[7]*AngloGold Ashanti Ltd, St Martins Tower 44, St Georges Terrace, Perth, WA 6000, Australia*

**Correspondence: mark.pearce@csiro.au*

Abstract: Microanalysis can provide rapid, quantitative characterization of mineral systems that complements the field- and core-scale observations traditionally made in ore deposits. We review recent innovations in microanalytical procedures and their application to studies of ore deposits. Case studies are presented examining how microanalysis can provide constraints on macroscopic processes within mineral systems. Synchrotron X-ray fluorescence shows centimetre-scale chemical variations associated with proximity to mineralization in samples from Sunrise Dam Gold Mine, Western Australia. Pseudomorphs of igneous plagioclase and chemically driven recrystallization interpreted from electron backscatter diffraction suggest that the system was dominated by fluid-driven brecciation with very little shearing. Both the fluid chemistry and fluid pressure evolved during a protracted sequence of vein formation and alteration accompanying gold mineralization. A second case study of sulphide mineralogy at the Mt Keith nickel sulphide deposit, Western Australia demonstrates how X-ray computed tomography combined with trace element mapping can constrain the chemistry and dynamics of magmatic systems. Large-scale interaction between silicate and sulphide melts, shown by homogenous palladium enrichment in pentlandite, leads to a large proportion of globular ores with a high nickel content. Increasing use of microanalysis in ore deposit geology is resulting in the constant reassessment of established models for ore genesis though a combination of micro- and macroscale datasets.

Mineral systems are complex environments in which a range of inter-related physical and chemical processes lead to the deposition of significant volumes of economically important minerals. The systems and processes that are important in understanding ore genesis occur at a wide range of scales, from lithospheric fault zones controlling fluid flow (Sibson *et al.* 1988; Hronsky *et al.* 2012) through bulk chemical and redox variations controlled by the lithostratigraphy (Evans *et al.* 2006) to individual grain interfaces that act as catalysts for deposition (Sung *et al.* 2009). It is therefore important that appropriate scales of observation are combined when seeking to understand the formation of ore deposits. Traditionally, the formation conditions of, and fluid characteristics responsible for, ore systems are inferred from vein parageneses and alteration assemblages based on core logging, hand sample evaluation and reflected light microscopy of selected samples. Although these techniques serve to address the decimetre- to metre-scale variability characteristic of many ore systems, quantitative

From: Gessner, K., Blenkinsop, T. G. & Sorjonen-Ward, P. (eds) 2018. *Characterization of Ore-Forming Systems from Geological, Geochemical and Geophysical Studies*. Geological Society, London, Special Publications, **453**, 7–39. First published online April 19, 2017, https://doi.org/10.1144/SP453.3

microscale analysis is increasingly being used in economic geology to provide constraints on mineral compositions and microstructures in both two and three dimensions. It is of vital importance to our further understanding of how ore deposits form that microscale observations are incorporated into models of ore-forming processes because these provide predictive capabilities and vectoring tools at the macroscale.

Microanalytical techniques are used to image and quantify chemical and structural variations of millimetre- to centimetre-sized volumes of material, typically with spatial resolutions better than 1 μm. When selecting an analytical technique to characterize the chosen samples, factors such as the type of data (chemical, structural or a combination), spatial resolution, detection limits, range of chemical elements available, destructive aspects and acquisition time must be evaluated. A summary of the spatial resolution and maximum practical observation scales for the techniques outlined in this paper is given in Figure 1. Some of the factors that dictate the maximum practical scales of observation and spatial resolution evolve as new analytical equipment is developed and it is thus often prescient to re-evaluate different techniques to see whether recent developments now offer the required resolution or increase in analysis rates.

Electron microbeam techniques (microprobe analysis and elemental mapping) have been used in geology for decades, but recent developments in both electron microscopes and detectors mean that collecting spatially constrained, high-quality data is now possible over relatively large areas in realistic time frames. Similarly, the lower limits of detection offered by laser ablation inductively coupled plasma mass spectrometry (LA-ICP-MS) and X-ray fluorescence (XRF) mapping mean that spatial variations in trace element content can now be quantified and mapped in both ore-forming and alteration minerals. Complementary data are available from ion beam mapping, which can be used for both trace element and isotopic analysis. The crystallographic relations of phases can be studied using electron back-scatter diffraction (EBSD) in a scanning electron microscope to identify the mineral replacement processes and to link mineralization to the deformation of the ore body. Mineral relationships in three dimensions are readily obtained using X-ray computed tomography (XCT). These data can be quantified to yield statistical parameters such as particle size distributions, connectivity and particle shape, which are useful for studies of ore-forming processes, geometallurgy or metal production engineering.

We review here the currently available microanalytical techniques that are being used to inform studies of ore-forming processes. For clarity and brevity, we limit the review to techniques that provide spatially constrained data rather than bulk analyses because this is where many advances applied to mineral systems have been made in the last decade. After a brief review of electron, X-ray, neutron, laser and ion beam based techniques, we present two case studies that demonstrate the utility of combining a number of complementary techniques to understand ore systems. We reflect on the developments that are currently coming on-stream and how these can be used to extend the multiscale approach to ore deposit studies to cover atomic to crustal scales.

Review of characterization techniques

We review here the techniques available to aid our understanding of ore deposits. The spatial resolution and practical spatial extent of each technique described are shown graphically in Figure 1. This information, along with details of sample preparation and the typical analytical resolution, is also given in Table 1. Many of the techniques outlined here can be carried out sequentially, generally with increasing spatial resolution. It should be borne in mind that non-destructive electron and ion beam techniques should be carried out before destructive techniques based on mass spectrometry that require the removal of material.

Electron microbeam techniques

Scanning electron microscopy (SEM) provides higher spatial resolution images than optical microscopy and can give qualitative and quantitative information on three-dimensional (3D) morphology, chemical composition, crystallographic orientation and speciation. Electrons from an incident beam with a known accelerating voltage interact with the surface of the sample and produce electrons and electromagnetic radiation (X-rays, visible light) characteristic of the minerals present. In this review, we concentrate on the quantitative analysis possible within the scanning electron microscope and the reader is referred to previous studies for information regarding different imaging techniques (Lloyd 1987; Watt *et al.* 2000; Ciobanu *et al.* 2011). It should be noted that although the principles of imaging with SEM have remained the same, developments in hardware and software now allow the rapid acquisition of images and chemical maps of entire thin sections at 50–100 nm resolution (Schumann *et al.* 2014). These can form the basis of more detailed imaging and microanalysis allowing the integration of centimetre- to micrometre-scale datasets.

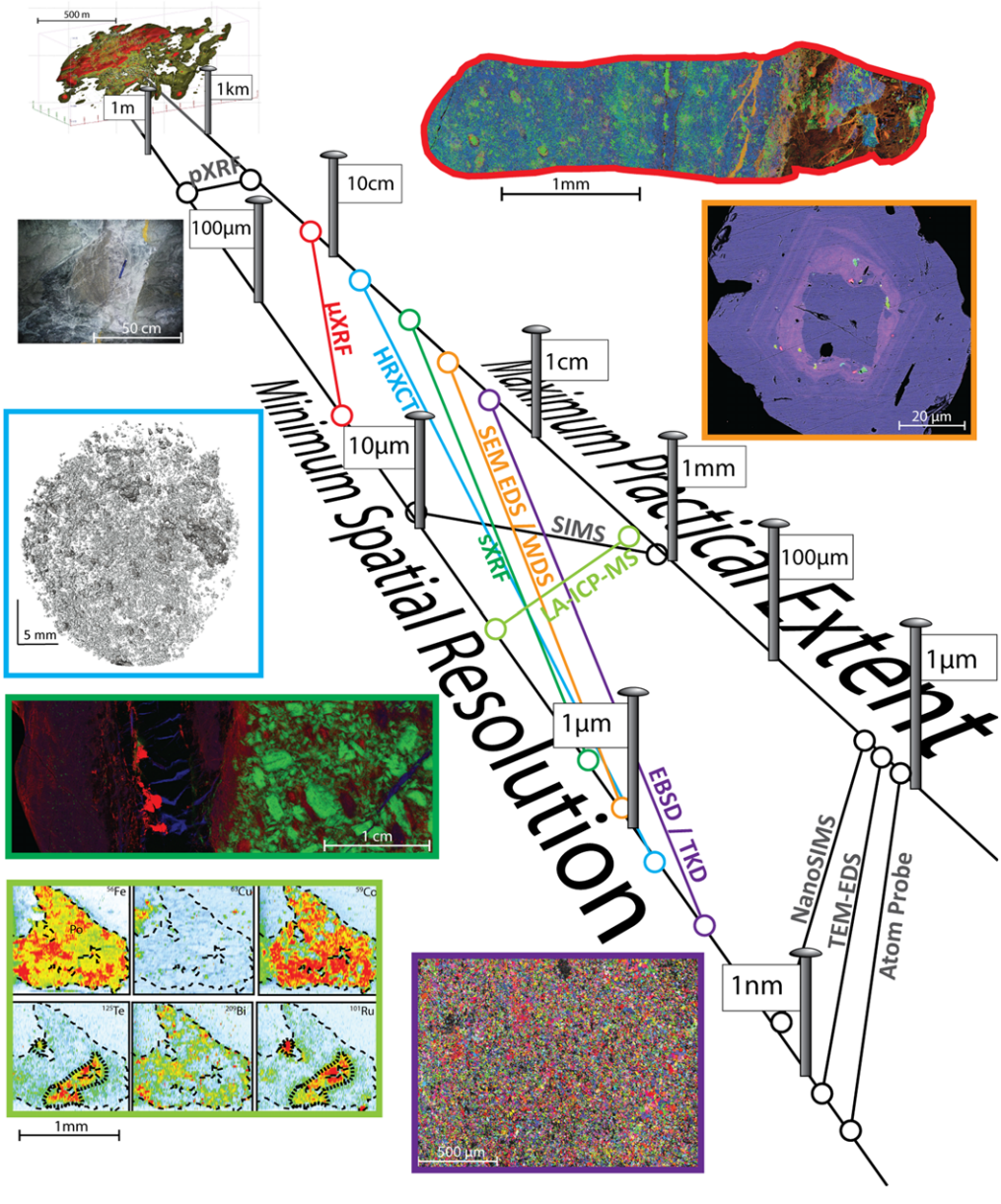

Fig. 1. Diagrammatic illustration of multiscale analysis. The minimum spatial resolution and largest practical aerial extent of each technique is shown joined by a tie line. The colours of the tie lines correspond to the outlines for each type of data. Note that larger extents are possible given sufficient time and money, but those illustrated are typically what is considered practical for a single dataset. Also, it may not be practical to collect data over the maximum spatial extent at the minimum resolution and a trade-off is often required directed by the question at hand. Spatial correlation between datasets of different resolution facilities our understanding of how microscale processes are manifested in core- to mine-scale datasets. Atom probe, atom probe tomography; EDS, energy-dispersive X-ray spectrometry; EBSD, electron back-scattered diffraction; HRXCT, high-resolution X-ray computed tomography; LA-ICP-MS, laser ablation inductively coupled plasma mass spectrometry; Nano-SIMS, nanoscale secondary ion mass spectrometry; pXRF, picoscale X-ray fluorescence; SEM, scanning electron microscopy; SIMS, secondary ion mass spectrometry; SXRF, synchrotron X-ray fluorescence spectrometry;TEM, transmission electron microscopy; TKD, transmission Kikuchi diffraction; µXRF, microscale X-ray fluorescence spectrometry; WDS, wavelength-dispersive X-ray spectrometry.

Table 1. *Summary of analytical techniques described in this paper*

Technique	Spatial resolution	Maximum practical extent	Typical analytical resolution	Sample type	Sample preparation	Data type	Notes
Portable X-ray fluoresence	1 cm	100s of metres at 10 cm intervals	ppm	Core, rock chips, powders	None	Chemistry – major and trace elements	Calibration with standards necessary for fully quantitative analysis; ensure trace elements in sample bags (e.g. arsenic in bleached paper envelopes) do not interfere with analysis
Micro-X-ray fluorescence	20 μm	10 cm	ppm	Cut and polished core, thin sections	Flat and polished sample surface, polished to 600 grit flatness	Chemistry – major and trace elements	
Synchrotron X-ray fluorescence	500 nm to 2 μm (depending on focusing ability of synchrotron)	5 cm	ppm	Thin sections, grain mounts, polished blocks/rock slices	Flat and polished sample surface	Chemistry– can be used for tomography	Depth resolution of heavy elements governed by thickness of sample
Energy-dispersive X-ray spectrometry scanning electron microscopy	1 μm (less for low keV)	5 cm	1000 ppm	Thin sections, grain mounts, polished blocks/rock slices	Flat polished sample with minimal topography; carbon-coated to prohibit charging of insulating rock samples	Chemistry – major elements	
Wavelength-dispersive X-ray spectrometry electron probe microanalysis	1 μm (less for low keV)	1 mm	10 ppm	Thin sections, grain mounts, polished blocks/rock slices	Flat polished sample with minimal topography; carbon-coated to prohibit charging of insulating rock samples	Chemistry – major and trace elements	
Proton-induced X-ray emission	2 μm	100 μm	ppm	Thin sections, grain mounts, polished blocks/rock slices	Flat and polished samples	Chemistry – major and trace elements	
High-resolution X-ray computed tomography	700 nm	7 cm	N/A	Core, single rock chips	Resolution governed by sample size so samples may need to be drilled to reduce total volume	Microstructure – attenuation structure interpreted in terms of density	Samples should be equant in directions perpendicular to rotation axis of tomography to limit artefacts arising from anisotropic attenuation
Cathodoluminesce	2 μm	1 cm (1 mm for hyperspectral)	ppm when calibrated with other techniques (e.g. laser ablation)	Thin sections, grain mounts, polished blocks/rock slices	Flat polished sample with minimal topography; thin (*c.* 5 nm) carbon-coated to prohibit charging of insulating rock samples, but ensure maximum emission of light	Trace elements, qualitative deformation (defect density)	Should be done early in analytical workflow because signal is very sensitive to any beam damage from other analyses

Laser ablation inductively coupled plasma mass spectrometry	10 μm	2 mm	ppt	Thin sections, grain mounts, polished blocks	Flat polished samples with minimal topography	Chemistry – trace elements, isotopes	Accurate quantification requires matrix-matched standards to account for instrument fractionation
Electron back-scattered diffraction	60 nm	5 cm	0.5°	Thin sections, grain mounts, polished blocks	Final polish with chemical mechanical colloidal silica (SYTON) polish for 1–4 h; soft phases may require milling with ion beam to remove polishing damage	Microstructure – crystallographic orientation	Poorly crystalline or easily damaged phases may not be analysed due to poor diffraction patterns
Transmission Kikuchi diffraction	5 nm	5 μm	0.5°	Transmission electron microscopy thin foils	Microstructures selected and prepared as thin (100 nm) foils using a focused ion beam, thinning of homogenous sample using ion beam milling	Microstructure – crystallographic orientation	Poorly crystalline or easily damaged phases may not be analysed due to poor diffraction patterns
Secondary ion mass spectrometry	10 μm	1 mm	ppb	Thin polished rounds, sections	Flat and polished, coated to reduce charge build-up	Chemistry – trace elements, isotopes	
Nanoscale secondary ion mass spectrometry	50 nm	5 μm	ppm	Thin sections, polished blocks	Flat and polished, coated to reduce charge build-up	Chemistry – trace elements, isotopes	Mass resolution is lower than for secondary ion mass spectrometry, so only applicable for large isotope variations (*c.* 1.5‰)
Energy-dispersive X-ray spectrometry transmission electron microscopy	1 nm	5 μm	1000 ppm	Transmission electron microscopy thin foils	Microstructures selected and prepared as thin (100 nm) foils using a focused ion beam, thinning of homogenous sample using ion beam milling	Chemistry – major elements	
Atom probe tomography	*c.* 1 Å	1 μm	<1 at.%	Needles *c.* 80 nm diameter at tip, 1–2 μm long	Focused ion beam milling of needles from thin sections or polished blocks	Chemistry – major and trace elements, some isotope information	

X-ray spectrometry

The best established SEM-based microanalysis technique is energy-dispersive X-ray spectrometry (EDX or EDS). A spectrum of X-rays is generated when incident electrons excite atoms within the sample and this spectrum contains peaks at energies characteristic of the elements present. Qualitative analysis using regions of interest in the spectrum gives the relative concentrations of elements, but is prone to error if peaks for different elements overlap or if significant pulse pile-up is present. Quantitative analysis involves fitting a background to the spectrum or removing it by filtering with a top-hat filter, deconvolving the elemental peaks as a series of Gaussian functions and then using the peak heights to determine the elemental concentrations. This method relies on the measured peaks being the same shape as the standard and being able to resolve overlapping peaks. Energy resolution has improved significantly as silicon drift detectors have replaced older silicon–lithium detectors, such that the energy resolution at manganese is now at the theoretical limit. This means that peaks which previously overlapped can now be successfully discriminated. In addition, the high throughput of the silicon drift detector spectrometers means that maps can be recorded at hundreds of thousands of counts per second, dramatically reducing analysis times. If the beam current and spectrometers are well calibrated and the sample is prepared correctly, then the sum of all elements present in an analysis should be within ± 1.5 wt% of the theoretical anhydrous total. Detection limits for this type of analysis are of the order of 0.1 wt% with analysis times typically of one to two minutes per point, regardless of the number of elements analysed. The X-ray spatial resolution is governed by the activation volume for the X-rays, which is a function of the composition and the accelerating voltage. The spatial resolution can be reduced to <100 nm at low accelerating voltages (e.g. 5–10 keV) depending on the X-ray line analysed. As the entire X-ray spectrum is collected for each pixel, unexpected elements can be identified during post-processing. Electron probe microanalysis (EPMA) using wavelength-dispersive X-ray spectrometry (WDX or WDS) can detect lower concentrations down to 100 ppm with a similar spatial resolution to EDS, but is generally more time consuming. A typical 10-element analysis on five spectrometers may take up to five minutes. If unexpected elements are present, then they will not be analysed, so EDS should be performed first. For many, if not most, applications that involve quantifying mineral compositions, the precision and detection limits offered by EDS are more than sufficient (Ritchie *et al.* 2012).

Rastering of the electron beam over the sample generates an X-ray spectrum at each pixel. Maps of elemental variation can be generated using spectrum regions of interest or by processing the spectra to provide semi-quantitative maps – for example, by deconvolving peak overlaps – or fully quantitative maps by quantifying the spectrum from each pixel. Software now routinely saves the spectra at each pixel, allowing post-processing and the analysis of spatial variation in unexpected elements. As the count times for each pixel in the map are generally less than for point analyses, the detection limits are significantly higher than for point analyses. However, the detection limits can be improved by binning data to increase the total counts or combining the counts from pixels that lie within a map region of interest to produce a better spectrum. These regions of interest can either be selected spatially or using statistical techniques such as principle components analysis (Kotula *et al.* 2003) or cluster analysis (Wilson & MacRae 2005) to aggregate similar spectra. The simultaneous collection of secondary and back-scattered electron images with EDS maps means that the two can be combined. This produces pseudo-high-resolution qualitative images of chemical variations with the spatial resolution of the electron image, but with the chemical information provided by the X-ray map. However, it should be noted that the actual resolution of the chemical data is not improved.

Elemental maps produced from EDS and WDS systems are used to show variations in major and minor elements in zoned minerals and to map the spatial distribution of different mineral phases. Warren *et al.* (2015) used maps of biotite composition modified by adjacent sulphides to show that major element modification can lead to changes in the trace element content and can potentially affect the utility of biotite as a vector in nickel systems. Combining maps of different elements as red–green–blue composite maps highlights the phase distribution more effectively than a single elemental map. In addition, the improved spatial resolution of EDS over optical techniques means that phase distributions can be examined at the micron scale, which is especially important when considering fine-grained alteration products (White *et al.* 2014; their fig. 8) or the intergrown clay/mica minerals common in hydrothermal mineral systems. Although the spatial resolution of EDS mapping might not be sufficient to obtain robust analyses of mineral phases, image analysis of the resulting maps can be used to calculate the relative mineral proportions to compare with the modelling outputs of large-scale fluid compositions (Pearce *et al.* 2015) depending on the scale of observations made.

Integrated automated mineralogy based on energy-dispersive spectrometry

Scanning electron microscopes with multiple EDS detectors operating in tandem can be used to produce phase maps from polished samples. These data can be used to examine the spatial distribution of different phases (Barnes *et al.* 2009; Zhao *et al.* 2012). As a result of time constraints, mapping is typically performed with spatial resolutions of 1–10 μm across a thin section and is used to rapidly acquire statistically robust datasets of mineral phase data (Gregory *et al.* 2013). The predominant use of these systems has been in ore processing, where the focus is to determine mineral liberation potentials, the proportion of ore mineral with the associated gangue, within crushed ore samples. Mineral liberation analysis software outputs the data in the form of particles that can be used to determine grain size, the complexity of the mineralogy of the ore and phase proportions. However, the rapid analysis of mineralogical maps across polished samples makes this type of analysis attractive to high-throughput data collection to fully characterize an ore system.

Cathodoluminesence

Cathodoluminescence (CL) uses the visible light generated by the incident electron beam in the same way as X-rays. It can be observed using an optical microscope, where the wavelength of the light corresponds to variations in colour. In the scanning electron microscope, depending on the spectrometers available, CL can be recorded as a combination of greyscale images of variations in light emission intensity, false colour images with a three-channel detector that detects set wavelength ranges, or as quantitative hyperspectral maps. The luminescence produced results from a combination of defects or activators within the crystal lattice, each of which results in a particular wavelength being emitted. It should be noted that cathodoluminescence signals are particularly sensitive to lattice defects and damage. Therefore CL analysis should be carried out as one of the first microanalysis techniques because the long dwell times and high beam currents associated with techniques such as EBSD and EPMA damage the crystal lattice enough to destroy the CL signal. CL images can be used qualitatively to show different generations of quartz dissolution and precipitation, interpreted in terms of pressure and temperature variations that cause variations in silica solubility (Rusk & Reed 2002). Combining CL and variations in the quartz trace element composition mapped using WDS and laser ablation leads to a more quantitative understanding of the cause of the variations in CL (Rusk *et al.* 2011; Leeman *et al.* 2012; Vasyukova *et al.* 2013). In the same way that each pixel in an SEM map is an entire spectrum that can be quantified, hyperspectral CL maps can be deconvolved to produce maps of variations in peak intensity for given activators. Once the peak positions have been calibrated using other analytical methods such as EPMA or laser ablation, the deconvolved maps give quantitative variations of not only trace element concentrations, potentially down to 10 ppm, but also concentrations of different oxidation states (MacRae *et al.* 2009). Applied to titanium in quartz thermometers (Wark & Watson 2006), hyperspectral CL mapping can provide high spatial resolution quantitative temperature estimates throughout ore deposits (e.g. Muller *et al.* 2003) much more rapidly than destructive laser or ion beam mapping of trace amounts of titanium (Leeman *et al.* 2008).

EBSD

EBSD is an SEM-based technique for measuring the crystallographic orientation of minerals. The sample normal is inclined at 70° to the incident electron beam and the diffracted electrons are recorded on a scintillator screen by a charge-coupled device camera positioned in front of the sample. Each set of lattice planes in the crystal being analysed produces a diffraction band and the pattern produced by all diffracting lattice planes is the resulting EBSD or Kikuchi pattern. Software then compares the pattern with theoretical solutions from a list of user-selected phases and solves for the best-fit phase and orientation of the crystal. Rastering a grid of measurements across a sample surface produces a map of varying orientations that can be analysed in terms of lattice strain and the crystallographic relationships between adjacent mineral grains (Prior *et al.* 1999). The spatial resolution of EBSD varies with the phase being analysed, but can be as small as 50–75 nm in metals, pyrite and olivine (Prior *et al.* 2009). Data acquisition rates have increased substantially in the last 10 years with the advent of parallel processing (one pattern can be acquired while other patterns are being indexed) and high-speed cameras. As such, polyphase, low-symmetry silicate samples that were previously limited to about five points per second can now be mapped at 30–50 points per second. Highly diffracting samples (e.g. metals and iron oxides) can be mapped at up to 550 points per second, making EBSD a fast, non-destructive technique for spatially constrained measurements of crystal orientations. As a result of increases in acquisition speeds, full thin section scale mapping is now practical at step sizes of 20–50 μm.

Most EBSD applications have been in deformed and metamorphosed rocks because variations in

crystallographic orientations lend themselves to the definition of the slip systems that operate during crystal plastic deformation (Prior *et al.* 2009). However, EBSD has also been applied to deformed ore deposits to constrain the timing of mineralization relative to deformation (Barrie *et al.* 2008; Reddy & Hough 2013; Rosiere *et al.* 2013) and to investigate trace element mobility in ore systems (Vukmanovic *et al.* 2014). The quantitative microstructural measurements that come from EBSD data, including the grain shape size distribution (Barrie *et al.* 2007; Vukmanovic *et al.* 2012), phase relations (Pearce *et al.* 2013) and internal strain (Barrie *et al.* 2007), make it an ideal tool to investigate the microstructural evolution of rocks during mineralization. In combination with high-resolution XCT, EBSD has also been used to investigate the crystallization mechanisms associated with igneous mineral deposits (Vukmanovic *et al.* 2012; Prichard *et al.* 2015).

The technique of EBSD is becoming more widely used to investigate the crystallographic controls on reactions during alteration and mineralization. Replacement reactions that occur in hydrothermal systems (Putnis 2009) often, but not always, show some degree of crystallographic correspondence between reactant and product minerals (cf. Xia *et al.* 2009; Zhao *et al.* 2009; Qian *et al.* 2010). Once the reactions and the reaction mechanisms are understood, they can be used to bracket fluid compositions and the volumes responsible for mineralization from numerical modelling (Pearce *et al.* 2015) or analogous experiments (Etschmann *et al.* 2014). Campbell *et al.* (2015) used EBSD combined with chemical analysis to demonstrate that a layer of pure supergene platinum formed on the surface of magmatic nuggets was microcrystalline and interpreted this in terms of the reactivity of platinum in the soil environment. Another common use of EBSD data in rock deformation is to examine the effects of crystallographic orientation on rock properties such as seismic anisotropy (Mainprice & Humbert 1994), piezoelectricity (Mainprice *et al.* 2014) and magnetic anisotropy. One of the major applications of this type of analysis is the study of the geophysical signatures of bodies, as exemplified by a study of seismic anisotropy in iron ore by Morales *et al.* (2008).

Current developments and nanoscale analysis

Many of the techniques outlined here have become commonplace in studying mineral deposits as a result of increases in the acquisition rates for good quantitative data. One other major frontier for analysis is increasing resolution and the interpretation of nanoscale data in the context of thin section to core-scale datasets. Focused ion beam (FIB) milling of site-specific microstructures enables features observed during microanalysis to be analysed in more detail using transmission electron microscopy (TEM) (see Ciobanu *et al.* 2011 for a review of the techniques). The X-ray mapping of TEM foils gives orders of magnitude increases in spatial resolution as a result of the reduced electron beam interaction volume. Ultra-bright electron sources and multiple EDS detectors enable rapid mapping at nanometre resolution. EBSD mapping can also be performed on thinned foils at *c.* 5 nm resolution (Trimby 2012), when it is known as transmission Kikuchi diffraction or transmission EBSD. It will be essential to incorporate nanoscale techniques into analytical workflows to understand trace element deportment (Deditius *et al.* 2011) and processes such as the remobilization, modification and transport of gold nanoparticles in ore-forming and weathering environments (Reich *et al.* 2006; Hough *et al.* 2011). A further increase in resolution can be gained by atomic-scale measurements made using atom probe tomography. The development of the laser pulse assisted atom probe (Bunton *et al.* 2006) makes this technique, previously restricted to metals, also available for insulating materials. Atoms are evaporated from a needle-shaped sample, made using an FIB, and recorded on a position-sensitive detector, thus allowing atomic positions to be reconstructed. The atomic species detected at a particular point is identified using time-of-flight mass spectrometry so that the spatial distribution of different types of atom can be examined. Successful results have been demonstrated in geological materials analysing the distribution of trace elements in zircon (Piazolo *et al.* 2016) to determine the extent and nature of radiation damage and verify the age obtained by ion probe analysis (Valley *et al.* 2014). As the volume of material examined by atom probe tomography is very small (needles are typically 100 nm in diameter and a few microns long), it is ideally suited to multiscale analysis. In ore systems, the hypotheses regarding trace element deportment (e.g. nanoparticulate v. solid-solution gold in sulphides; Fougerouse *et al.* 2016*b*) and pathfinder element mobility (Vukmanovic *et al.* 2014) can be tested and the results applied to larger scale detection methods, such as core-scale portable XRF spectrometry.

Another area of rapid development has been in detection and the energy resolution of SEM-based X-ray spectrometry. The spectral resolution offered by regular silicon drift detectors is improved by using windowless systems that can detect and quantify the Li Kα peak at 56 eV. Coupled with a cold field-emission scanning electron microscope that can achieve high spatial resolutions of a few nanometres using accelerating voltages as low as 0.1 keV, these new developments offer exciting

opportunities in micro- and nanoanalysis (Demers *et al.* 2013).

XRF mapping techniques

Proton-induced X-ray emission and bench-top micro-XRF

XRF techniques have traditionally been applied to the bulk analysis of geological samples. More recently, however, the application of micro-XRF (μXRF) to elemental imaging, both qualitative and quantitative, has become increasingly common. Both laboratory-based instruments and synchrotron facilities allow the collection of μXRF datasets.

Proton-induced X-ray emission (PIXE) imaging of samples has been widely used to study mineral systems. The passage of an energetic (several MeV) proton past atoms in the sample can lead to the ionization of electrons in the inner atomic shells. The subsequent filling of the resulting inner shell vacancies by atomic transitions from the outer shells leads to the emission of characteristic X-rays for each element. At the same time, the deceleration of the proton in the sample is slow and leads to low levels of continuum background. With its high X-ray production yields and low continuum background, PIXE provides good detection limits for all elements heavier than Z_c 13 (aluminium). Typical detection limits reported in silicate and sulphide minerals are around 1–2 ppm for a five minute analysis time. Longer counting times yield detection limits down to 0.3 ppm (Ryan 2001). Spot sizes of 1–2 μm can be achieved. PIXE is a simultaneous, multi-element technique. This means that any element present above the detection limits will be seen, analysed and imaged. Therefore it is not necessary to preselect the elements of interest in a particular sample suite. Like most ion beam techniques, PIXE is non-destructive. Therefore the sample is neither destroyed nor consumed in the analysis and can subsequently be characterized by other methods. This also means that there is no fallout or debris that can contaminate other parts of the sample (Ryan *et al.* 1995; Ryan 2000).

PIXE has been used to inform our understanding of the processes forming mineral systems by the analysis of mineralizing fluids preserved in fluid and melt inclusions (Ryan *et al.* 1995; Baker *et al.* 2006; Baker *et al.* 2008; Xie *et al.* 2009). The analysis of fluid inclusions in mineral system samples can inform our understanding of ore-forming processes. PIXE analysis of fluid inclusions provides a direct, non-destructive method to determine the composition of these trapped fluids and allows identification of the elements that reside within the fluid inclusions, as well as the discrimination of the solid phases outside and in close proximity to the inclusions (Ryan 2000).

The direct analysis of trace element variations in the ore and gangue minerals (Petrie *et al.* 2005; Yeats *et al.* 2010) also provides insights into ore-forming processes, allowing the discrimination of multiple phases of sulphide formation, the relationship of those phases to the timing of key ore metal deposition and the study of variations in elemental concentrations caused by fluid mixing in the formation of black smokers.

The development of bench-top XRF imaging systems has allowed for large area (up to 15 × 20 cm) element mapping of hand specimens with reported spot sizes of >25 μm. Le Vaillant *et al.* (2015, 2016) demonstrated the use of μXRF mapping of core samples to understand the local-scale mobilization of elements at the Kevitsa and Mittel nickel sulphide deposits. The core-scale element imaging supported the discovery of a geochemical halo around the deposits created by the hydrothermal remobilization of base metals, gold and platinum group elements (PGE) into the rocks surrounding the mineralization. The analysis of the Kevitsa samples at centimetre to metre scales was combined with assay data collected at regional scales to inform our understanding of the variability in scales over which elements of interest were mobilized (Le Vaillant *et al.* 2016), with gold and copper found to be more mobile and therefore more likely to have been redistributed by hydrothermal fluids.

Synchrotron μXRF and X-ray absorption near-edge spectroscopy

Synchrotron-based μXRF allows the *in situ* mapping of elements at nanometre to micron scales. As with other XRF techniques, it is non-destructive and has further benefits over SEM and electron beam techniques in that it requires minimal sample preparation, reducing the potential for the introduction of artefacts and allowing analysis under ambient environmental conditions. The simultaneous imaging of multiple elements is possible with no preselection required.

The development of the Maia detector array and integrated real-time processor to acquire elemental maps using XRF microscopy has allowed the scanning of complex natural samples over 100–200 mm^2 at a spatial resolution of 2 μm (Paterson *et al.* 2011), with typical image sizes of 10–100 megapixels acquired over two to ten hours. The collection of such datasets supports the recognition of textural and chemical variations over four orders of spatial scale (Ryan *et al.* 2014). The greater penetration depth, coupled with the wide-angle array, allows the depth resolution of discrete particles, which may only be at ppb concentrations in the

bulk composition (Dyl *et al.* 2014; Maier *et al.* 2015; Barnes *et al.* 2016; Li *et al.* 2016), whereas the relatively low detection limits and high spatial resolution allow the quantification of subtle mineral zoning (Barnes *et al.* 2011). The XRF data collected with the Maia detector array are processed using the computationally efficient dynamic analysis method (Ryan *et al.* 2005) to deconvolve complex spectra that often contain many overlapping peaks. The precise determination of elemental concentrations using this method relies on selecting a matrix material close to that being analysed so that the peak shapes are similar in the computed matrix file and the experimental sample. As a result, iterative procedures for pixel-wise analysis using a variable matrix are currently under development (Ryan *et al.* 2015).

The tunability of incident X-rays from a synchrotron radiation source allows the collection of X-ray absorption near-edge spectrometry (XANES) data, thus providing *in situ* data on element speciation. The capability of the Maia detector for imaging to around 10^8 pixels supports XANES imaging, where the production of images up to *c.* 10^6 pixels can be repeated over 100 times with step changes to the beam energy through an absorption edge to collect a dataset from which chemical state images can be projected (Etschmann *et al.* 2010). An individual XANES spectrum consists of the pre-edge energies, the absorption edge for the element of interest and the post-edge spectrum. The exact energy at which the excitation occurs (the white line energy) is affected by the oxidation state of the element. Comparison of the experimental spectra with standards of known oxidation state allows determination of the experimental oxidation state, or deconvolution of the spectrum in the case of mixed valence states. The post-edge region (the absorption spectrum at energies higher than the excitation edge) contains a structure (the X-ray absorption fine structure) related to the electronic environment of the element being analysed, e.g. the bonding environment within a mineral or the coordination number with aqueous ligands in solution). The Fourier transform of the X-ray absorption fine structure part of the spectrum gives the bond lengths of the atoms under consideration. In studies of ore deposits, the oxidation state of trace elements incorporated in hydrothermal minerals can provide a constraint on the chemistry of ancient fluids that cannot be directly sampled and can improve our understanding of the mechanisms responsible for mineral precipitation (Brugger *et al.* 2010).

XCT

XCT is a non-destructive method originally developed and used as a medical imaging technique (Hounsfield 1973). It allows the reconstruction and visualization of the internal structure of solid objects in three dimensions. Typically, a micro-focus X-ray beam source illuminates the sample and a sensitive X-ray detector collects projections (radiographs) of the sample at different angles. These projections are then used to reconstruct a regular volumetric grid (with an isotropic or anisotropic voxel size depending on the scanner setup) where each voxel has a unique greyscale value that is a function of the attenuation of the X-ray across the material. The attenuation of X-rays within the samples largely depends on the mean atomic number, the density of the material and the spectral characteristics of the X-ray source; see Godel *et al.* (2006) and Godel (2013) for further details on the principles.

The range of X-ray energies used enables transmission through complex and dense materials, including ores. Data can be acquired with limited to no preparation on samples within a range of resolutions using two different types of scanner. Low-resolution data (>500 μm spatial resolution) can be acquired on samples varying in size from a few centimetres up to an entire drillcore length using conventional medical CT scanners. This type of scanner allows rapid data acquisition (a few metres of drillcore per hour), with a range of voltages and intensities possible from 70 to 140 kV and up to 800 mA, respectively. However, the absence of a filter, the range of energies used and the spatial resolution achievable limit the ability to differentiate complex mineral assemblages and hence it only gives a broad overview of the ore materials. As a result, in most cases, high-resolution X-ray CT (HRXCT) data have to be acquired on a smaller sample (up to *c.* 5 cm in diameter and *c.* 10 cm in length) to allow quantification. Recent HRXCT scanners have the ability to generate multiscale (25 down to 0.3 μm voxel size) imaging of a given sample. The wide range of voltage, current, power, filters, source and detector position combinations make it possible for modern HRXCT scanners to scan a wide range of materials for mineral system studies at high resolution (from tree leaves and pressed powder to samples containing large gold particles). The data generated by HRXCT not only provide some striking 3D images, but can also be processed and analysed using dedicated workflows and algorithms. The processed datasets provide *in situ* quantitative 3D mineralogical and textural measurements that are impossible to assess accurately by any other method; see Godel (2013) and references cited therein for further details. This new information can be directly used for scientific studies to understand the origin of a given ore body, but can also can be used for mineral processing applications to facilitate the recovery of metal resources or improve the metal extraction efficiency.

The use of XCT in ore geology and mineral system science has increased significantly over the past decade and applications encompass a wide range of commodities (e.g. gold, PGEs, nickel, copper, iron ore, chromium, titanium and graphite). Early studies on gold (Kyle & Ketcham 2003), PGE sulphide ores (Godel *et al.* 2006) and nickel sulphide ores (Barnes *et al.* 2008) mostly used XCT as an observation platform, with quantification limited to calculating the 3D distribution of phases of interest and their volumes (Kyle & Ketcham 2003). Although XCT is still used to generate a stack of two-dimensional images for observation, there is a shift towards more detailed 3D analysis and quantification. HRXCT has notably been used:

(1) to assess the gold grade in samples from the Grasberg porphyry copper–gold ores in Indonesia (Kyle *et al.* 2008);
(2) to quantify the size and 3D textural relationships of platinum group minerals in ores from the Bushveld (South Africa) and Stillwater (USA) complexes, with implications for ore-forming processes (Godel *et al.* 2010; Godel 2015);
(3) to assess the variability in palladium tenor of sulphide droplets as a function of their 3D textural relationship with iron–titanium oxides and silicate minerals in samples from the Platinova Reef of the Skaergaard intrusion in Greenland, with implications for ore genesis (Godel *et al.* 2014; Holwell *et al.* 2016);
(4) to assess the variability in sulphides and sulpharsenide 3D morphology as a function of their PGE concentrations in samples from the Rosie Nickel Prospect in Western Australia, with implications for the geochemistry of PGEs in sulphur–arsenic systems, ore genesis and noble metal (platinum and palladium) recovery (Godel *et al.* 2012*b*);
(5) to quantify the 3D distribution, size, morphology and degree of interconnectivity of a komatiite-hosted magmatic nickel sulphide to provide new insights into the deposition of magmatic nickel sulphides (Godel 2013; Godel *et al.* 2013);
(6) to quantify the porosity and pore characteristics and mineralogical proportions in natural iron ore samples, with implications for geometallurgy (Fonteneau *et al.* 2013);
(7) to locate silicate inclusions in iron–titanium oxides, with implications for the formation of the Baima iron–titanium oxide deposits in China (Liu *et al.* 2014);
(8) to quantify the volume proportion of tungsten and its grade in scheelite-bearing samples, with benefits for metal recovery (Le Roux *et al.* 2015);
(9) combined with EBSD to image the crystal structure of an ophiolitic nodular chromite ore (Prichard *et al.* 2015); and
(10) to determine chromite morphology in komatiite-hosted nickel sulphide deposits (Godel *et al.* 2012*a*) and PGE reefs to constrain ore genesis (Vukmanovic *et al.* 2012).

Ion beam techniques

Secondary ion mass spectrometry

Secondary ion mass spectrometry (SIMS) is a surface to small volume (<1 μm in the third dimension) analysis technique that uses a beam of primary ions (usually Cs^+ or one of O^-, O_2^- or O^+) to sputter the sample surface and create a stream of secondary ions. The secondary ions (and some back-scattered primary ions) are delivered into a mass spectrometer to determine the trace elements or isotope ratios for the system of interest. Specialist instruments with a high mass resolution – spatially high-resolution ion microprobe (SHRIMP) – are able to distinguish uranium and lead isotopes and are used to provide high-precision dates from zircon U–Pb geochronology by spot analyses. Smaller radius instruments, e.g. the Cameca IMS 1280, have the ability to raster the primary ion beam to image variations in trace elements and spatial variations in isotope ratios. The versatility of SIMS in terms of elemental range (from hydrogen to uranium on most systems) and the ability to measure isotope ratios and trace elements with ppb detection limits for many elements makes it an excellent choice for mapping mineral chemistry. Insulating samples need to be coated with gold or carbon to reduce charge build-up and are commonly thin discs, although individual instruments vary. The spatial resolution of SIMS is governed by the extent to which the primary ion beam can be focused. SIMS spots are typically of the order of 20–30 μm (with accelerating voltages of up to 10 keV), but can be more finely focused at lower voltages. Increased spatial resolution is gained by a NanoSIMS instrument, which uses a similar caesium or oxygen ion beam, but an altered focusing setup allowing resolutions of 50 nm (with a Cs^+ beam). Although NanoSIMS is also capable of trace element mapping and isotopic analyses, natural isotope ratios are generally not large enough to be differentiated with NanoSIMS (Kilburn & Wacey 2014), with the exception of sulphur isotopes (Zhang *et al.* 2014*a*) and in isotopically doped experimental products where the isotope ratio variations are much larger. Therefore NanoSIMS is commonly used in exploration geoscience to map trace elements where the scales of variation are commonly <10 μm.

SIMS and NanoSIMS have been used to map low levels of gold in sulphides (Simon *et al.* 1999; Steele *et al.* 2000) as well as the associated changes in sulphur isotope composition of pyrite (Barker *et al.* 2009) and trace element contents (Chouinard *et al.* 2005). These techniques together constrain the composition and source of the ore-bearing fluids. Variations in the gold concentration in arsenopyrite that were initially observed in synchrotron XRF maps were further imaged by NanoSIMS and used to infer the local-scale remobilization of gold during late-stage fluid flow in the Obuasi deposit, Ghana (Fougerouse *et al.* 2016*a*).

Laser techniques

LA-ICP-MS analysis and mapping

LA-ICP-MS is a destructive technique that allows the quantification of a wide range of trace elements in ore materials down to ppb levels. A pulsed laser beam ablates the surface of the sample to create aerosols that are transported in the ICP to generate ions, which are then separated and collected according to their mass to charge ratios. The trace element concentrations can be recalculated with high precision and accuracy providing that suitable (matrix-matched) reference materials have been analysed during each experiment to correct for instrument drift and potential interference. Any type of flat and solid sample can be analysed with limited sample preparation. Current sample holders accommodate a wide range of sample sizes.

The LA-ICP-MS systems can be used in two different modes: (1) using spot analysis (spot sizes typically ranging from *c.* 4 to 100 μm) where the laser beam drills through the samples at a given speed (depending mainly on the material ablated, the energy and the frequency used); or (2) using a rastering technique where the laser beam moves at a given speed along a path at the surface (with an ablation depth of a few micrometres in most cases) of the sample. Both modes can be used to provide semi-quantitative to quantitative trace element maps of a region of interest with spatial resolutions down to *c.* 10 μm.

The vast majority of the studies that use LA-ICP-MS analysis focus on the application of the method to determine the partitioning behaviour of trace elements in given mineral phases, with implications for ore-forming processes and metal recovery. LA-ICP-MS analysis using the spot mode was originally used in ore geology to determine the trace elements in a range of sulphide and arsenide minerals from various deposits types such as PGE and nickel–copper ores (Huminicki *et al.* 2005; Barnes *et al.* 2006; Godel *et al.* 2007; Holwell & McDonald 2007; Godel & Barnes 2008; Dare *et al.* 2010; Dare *et al.* 2011; Pina *et al.* 2012) and gold (Large *et al.* 2007; Large *et al.* 2009; Thomas *et al.* 2011). More recent studies cover a wider range of deposits (lead–zinc, volcanogenic massive sulphide or iron oxide–copper–gold deposits) and in most cases combine semi-quantitative LA-ICP-MS mapping with quantitative spot analysis (Cook *et al.* 2011; Cook *et al.* 2013; Zhang *et al.* 2014*b*; Duran *et al.* 2015; Gadd *et al.* 2015; Genna & Gaboury 2015; Lawley *et al.* 2015; Meffre *et al.* 2015). Owing to the complexity of the data acquisition and processing, only few studies have reported methods to provide truly quantitative maps (Paul *et al.* 2014; Lawley *et al.* 2015).

Case studies applying microanalysis to mineral systems

Having discussed recent advances in the microanalytical techniques available to study mineral deposits, we now outline two case studies that apply a combination of these techniques to understanding the processes that have led to the deposition of ore minerals and their associated alteration. The first example applies synchrotron XRF, SEM-based EDS and EBSD to examine the cyclic fluid flow and deformation events that led to the formation of Sunrise Dam Gold Mine (SDGM), Western Australia. The second example examines the particle size distribution within the Mt Keith nickel sulphide deposit, Western Australia using HRXCT and couples this with variations in the trace element chemistry of sulphides.

Case study 1: vein formation, alteration and gold mineralization at SDGM, Western Australia

Geological background

The SDGM is located 55 km south of Laverton (29° 05′ S, 122° 25′ E) in Western Australia, within the Laverton Domain of the Kurnalpi Terrane of the Yilgarn Craton. The SDGM ore bodies sit within the structurally complex Laverton Domain and are hosted in a sequence of shallow-dipping Archaean metasedimentary and metavolcanic rocks, intruded by dolerite and porphyritic microgranite and granite (Newton *et al.* 1998). The metavolcanic rocks are interbedded with banded iron formation units. The region has undergone lower to mid-greenschist metamorphism (Hallberg 1985) and multiple deformation events (Baker *et al.* 2010). An early stage of extensional deformation was followed by several phases of compressional deformation (Nugus *et al.*

2005; McLellan *et al.* 2007). Mineralization is predominately hosted within andesitic rocks, which are variably altered. Gold mineralization is largely associated with shear zones and breccia zones active during the later stages of compressional deformation (Blenkinsop *et al.* 2007; Nugus *et al.* 2009). Mineralization is hosted in shear zones and stock works and the majority of the gold is localized within veins.

Gold mineralization is associated with alteration characterized by the breakdown of plagioclase at the expense of sericite ± carbonate–pyrite–silica. Multiple populations of arsenian pyrite and arsenopyrite are associated with distinct stages of deformation (Sung *et al.* 2009), with later populations hosting higher concentrations of gold. At submetre scales, some high gold grades are hosted in veined samples with minimal alteration, while some intensely altered rocks contain little gold.

Complex and mutual cross-cutting relationships are observed in the multiple vein populations. Oliver *et al.* (2012) explained the overprinting vein observations as being a result of a feedback mechanism between alteration and cracking in which the geochemical change associated with alteration caused a reduction in porosity, an increase in pore pressure, re-cracking and the deposition of the highest grades of gold in rogue cracks. The cycling of pressure through both over- and underpressured regimes is supported by fluid inclusion results that document rapid phase changes associated with seismicity (Brown *et al.* 2003; Baker *et al.* 2010).

In this case study we build on the framework of deformation and fluid flow established by detailed field observations, fluid inclusion analysis and microstructural studies of sulphide-hosted gold to examine: (1) the scales of element mobility during fluid-driven alteration by examining trace elements within and across alteration halos with synchrotron XRF; and (2) the cyclic evolution of brittle and ductile rheology using EBSD to constrain deformation styles within wall rocks and veins. Examining these important parameters will enable us to constrain the relative importance of the chemistry and rheology in forming giant gold deposits such as that at the SDGM.

Samples and analysis techniques applied to SDGM samples

To investigate the microstructural and microchemical changes characteristic of large-scale fluid pressure cycling and vein-hosted high-grade gold mineralization, three samples from the GQ lode of the SDGM were studied. The GQ lode is found within altered greenschist facies andesite lavas and volcanic rocks. The samples (GQ1, GQ2 and GQ3) were collected from a drive wall on the 1943 level, 79E and are increasingly proximal to a decimetre-scale vein and the accompanying alteration selvedge, faults and fractures (Fig. 2). Chemical and microstructural data were collected using the following techniques and conditions. A progressive reduction in the scale of analysis (from outcrop to centimetre- and micrometre-scale analyses) led to the progressive refinement of the hypotheses presented here. This study combines chemical data from XRF and EDS with microstructural analysis by EBSD to understand the interaction between physical and chemical processes. Synchrotron XRF maps were collected on the XFM beamline at the Australian Synchrotron using a Maia 384 detector, an 18.5 keV monochromatic incident X-ray beam, a step size of 4 μm and a dwell time of 0.97 ms per pixel. Details of the detection limits for these samples can be found in Fisher *et al.* (2015). The data were processed using GeoPIXE (Ryan *et al.* 2002), assuming a matrix of muscovite, to calculate the corrections for absorption and the fluorescence yield of X-rays. This dataset was used to produce Figure 6c and f. To calculate the composition of the pyrite accurately, the raw data were reprocessed assuming a pyrite matrix. These data were used to produce Figure 6d and e. Full resolution versions of the synchrotron XRF maps are available through the CSIRO Data Access Portal (Fisher & Ryan 2014; Pearce *et al.* 2016). EBSD mapping was carried out using a Tescan Mira field-emission gun scanning electron microscope and Oxford Instruments AZtec 3.0 software, a NordlysNano EBSD detector, an accelerating voltage of 20 keV and a step size between measurements of 1 μm, acquired at a rate of *c.* 40 patterns per second. The resulting map covers 1.8 × 1.35 mm and contains 2.43 million pixels. During acquisition, 67% of the acquired patterns were successfully indexed. Post-processing was carried out based on band contrast constrained interpolation (Prior *et al.* 2009) using EBSDinterp software (Pearce 2015). This step reduced the number of non-indexed points to 30%. Detailed mapping was subsequently carried out at 580 nm step sizes to examine in detail the grain size variations within the microstructure. The raw EBSD data and processing parameters are available through the CSIRO Data Access Portal (Pearce & Reddy 2016). The chemistry of the samples was mapped using a Bruker XFlash EDS detector and either a Philips XL40 W-filament scanning electron microscope (operating at 30 keV) or a Zeiss UltraPlus field-emission gun scanning electron microscope (operating at 20 keV, 1.2 nA). Two parts of the most altered sample (GQ3) were scanned using HRXCT (using a XRADIA XRM 500 3D X-ray microscope) to investigate changes in sulphide populations.

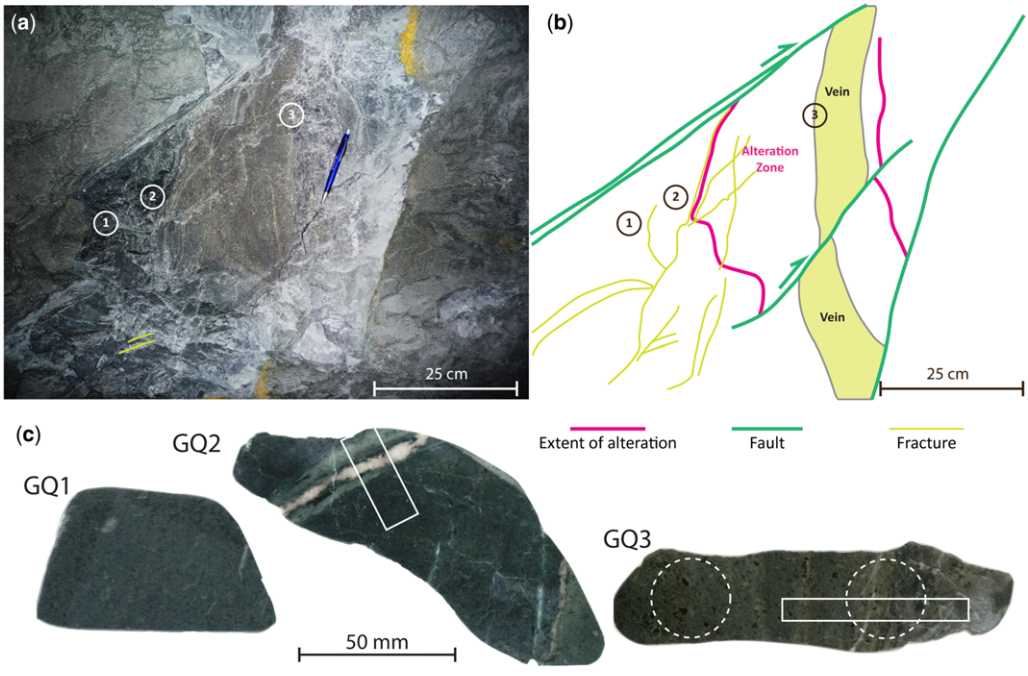

Fig. 2. Locations and sample images for three Sunrise Dam samples. (**a**) Outcrop photograph showing sample locations (GQ1, GQ2 and GQ3) in relation to decimetre-scale veining and minor faulting. (**b**) Sketch outline of photograph in (a) showing fractures (yellow), faults (green) and alteration zones (pink) and the vein. (**c**) Scanned, cut-polished slabs from three samples of varying intensity of alteration. White boxes show the location of synchrotron XFM datasets in Figure 4 (GQ2) and Figure 6 (GQ3). White dashed circles show the locations of the two high-resolution X-ray computed tomography datasets in Figure 7.

Results

Sample GQ1 is the least altered of the samples and contains sericite pseudomorphs after plagioclase and chlorite after amphibole or biotite. The euhedral feldspar pseudomorphs can be seen clearly in the back-scattered electron montage, along with subhedral pyrite (Fig. 3a). Chemical maps of the matrix (Fig. 3b) show fine-grained intergrowths of chlorite, quartz, rutile and calcite. There is calcite and fine-grained chlorite within the feldspar pseudomorphs. The association of chlorite and rutile suggests that chlorite results from the breakdown of biotite.

Sample GQ2 is slightly more proximal to the mineralization than GQ1 and has two microstructurally distinct parts (Fig. 4). One domain (pseudomorphed domain) contains sericite pseudomorphs after plagioclase similar to GQ1 (compare Fig. 3b, c) and chlorite after biotite or hornblende. The second domain is a more homogenous zone developed asymmetrically around a quartz vein (Fig. 2) and appearing like an alteration selvedge. The homogenous domain is more manganese-rich than the heterogeneous domain, with a thin manganese-rich selvedge to the quartz vein grading diffusely into the heterogeneous domain (the extent of this diffuse manganese-rich area is highlighted by a dotted line in Fig. 4). The vein is cut by later calcite ladder veinlets (strontium-bearing in Fig. 4a) and contains pyrite (bright red in Fig. 4). Muscovite porphyroblasts are developed in the homogenous domain (green flecks in Fig. 4a), which otherwise consists of chlorite, quartz and dolomite. Titanium (as rutile) and zirconium (distributed in the silicate phases) are present in the heterogeneous domain, but are absent from the homogenous domain (Fig. 4b).

The microstructure of the homogenous domain, which is predominantly dolomite and quartz, was detailed by EBSD. The map shows that the homogenous domain is composed of both polyphase and single-phase regions (Fig. 5a). As well as phase information, EBSD provides the crystallographic orientation at each measurement point (Fig. 5b–d). Processes such as oriented growth or deformation can result in the alignment of crystals to produce a crystallographic preferred orientation (CPO). A CPO is most easily observed by plotting pole figures (or contoured stereograms) or crystallographic axes and looking for concentrations that are higher than expected for a random distribution (contour

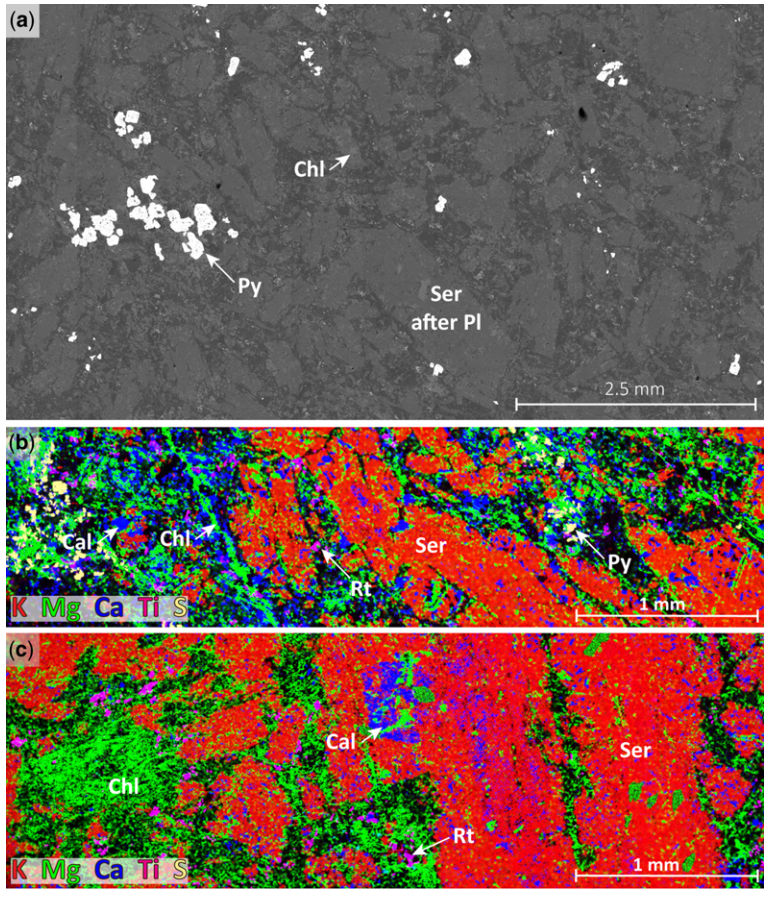

Fig. 3. Microstructures of alteration samples. (**a**) Back-scattered electron montage image of a large area of sample GQ1 showing pseudomorphed plagioclase phenocrysts in a matrix of chlorite, quartz and calcite. Image consists of 110 individual images stitched together and took about one hour to acquire. Composite elemental maps of energy-dispersive X-ray spectrometry chemical data showing spatial variations in potassium (red), magnesium (green), calcium (blue), titanium (pink) and sulphur (pale yellow) in (**b**) sample GQ1 and (**c**) the matrix of GQ2. Spatial resolution is *c.* 2 μm. Each image is a montage of two maps that took about two hours to collect. Large muscovite pseudomorphs after plagioclase are associated with calcite. A finer grained matrix of mafic minerals (biotite or hornblende) have been pseudomorphed by chlorite. Datasets were mapped at a 2 μm pixel spacing to show the fine-grained intergrowth of minerals that result from replacement.

values as multiples of a uniform distribution (MUD) >1). The overall preferred orientations for the quartz and dolomite in the homogenous domain are close to random (maximum MUD values of *c.* 1; Fig. 5b). Detailed maps for the polyphase and single-phase domain are shown in Figure 5c, d, where the grains are coloured by their orientation. Patches of dolomite grains with a similar orientation (similar colour) are present in the polyphase domain (examples highlighted on Fig. 5c) and these show stronger CPOs with maximum MUD values >6 (Fig. 5g, h).

Orientation measurements can also be used to determine grain boundaries, across which the orientation change is greater than a threshold value (10° in this study) and give the grain size distribution for each phase (Fig. 5e, f). In the polyphase domain, the quartz and dolomite have a similar mean grain size around 5 μm. In the single-phase, quartz-rich domain, the mean quartz grain size (7.1 μm) is larger than that of dolomite (4.3 μm).

Sample GQ3 is the most proximal sample to the decimetre-scale vein (Fig. 2) and contains part of a vein and native gold. Micro-XRF mapping of the entire sample (Fig. 6) shows that pyrite is present throughout the sample (green in Fig. 6b) and the rock is also strongly sericitized (blue in Fig. 6b). There is extensive dolomite/ankerite veining

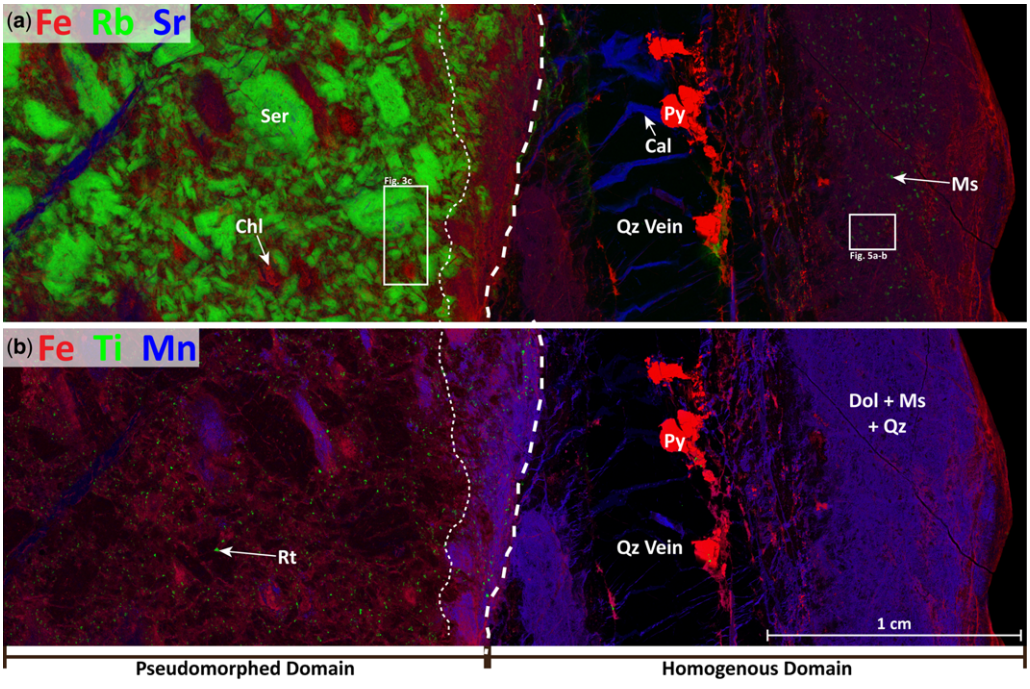

Fig. 4. Red–green–blue composite maps of synchrotron XFM data from sample GQ2. Map produced from a dataset of 33.1 megapixels collected in about nine hours with a step size of 4 μm and a dwell time of 0.98 ms/pixel. (**a**) Iron (red), rubidium (green) and strontium (blue) highlights show the sample has two microstructural domains. Pseudomorphed domain: igneous textured with large sericite pseudomorphs after plagioclase that concentrate rubidium and iron-bearing chlorite. Homogenous domain: developed asymmetrically around a quartz vein containing muscovite porphyroblasts. The quartz vein is cut by later calcite veins (containing strontium) with minor dolomite and is associated with pyrite on one margin. White boxes show approximate locations of the energy-dispersive X-ray spectrometry map in Figure 3b and the electron back-scattered diffraction dataset in Figure 5. (**b**) Iron (red), titanium (green) and manganese (blue) show chemical alteration (manganese addition) around the quartz vein. The titanium grains are ubiquitous in the pseudomorphed domain and completely absent in the homogenous domain. Dotted line shows the edge of the manganese-enriched domain on the wall rock side of the vein.

(iron + calcium; orange in Fig. 6b) at the margin with the main quartz vein and there are pieces of pyrite- and sericite-bearing wall rock within the quartz vein itself. The pyrite shows two distinct microstructures within the wall rock (Fig. 6c). One microstructure has finer grained pyrite in chlorite interspersed with centimetre-scale patches of sericite (rubidium-bearing in Fig. 6c) and chlorite. Adjacent to this are coarser grained pyrites nucleated on quartz-rich veins, surrounded by sericite selvedges that are completely devoid of pyrite and chlorite. Titanium-bearing grains are distributed uniformly throughout the microstructure.

The pyrite grains in GQ3 have variable arsenic contents. Assuming that similar pyrite trace element compositions grew at the same time, a marker composition has been selected to compare pyrite populations based on their copper and arsenic contents (Fig. 6d, e). Pyrite with 0.03–0.2 wt% As and 0.0004–0.03 wt% Cu is highlighted in green on Fig. 6d. The exact compositional range used is shown in the white outline in Figure 6e. The element combination plot shows copper and arsenic values for all pixels in the entire map with high copper and arsenic in tennantite (not shown). Most of the pyrites have low copper and arsenic contents. The high arsenic values highlighted in Figure 6d are found within a thin band in the large pyrites and more widely distributed in the fine-grained pyrite.

Sulphide distribution between gold-bearing and barren samples was examined using HRXCT (Fig. 7a, b). Two 25 mm round samples were taken from sample GQ3. One was from the gold-bearing part and the other from the opposite end of the sample (*c.* 10 cm away). Crystal sizes distributions are plotted as equivalent spherical diameter of the sulphide aggregates (Fig. 7c, d). The unmineralized

sample contains a uniform number of particles of diameter <1200 μm, with very few particles larger than this. In the gold-bearing sample particles >1200 μm are more prevalent and there is a decrease in the proportion of particles with diameters between 600 and 1200 μm relative to the unmineralized sample.

Cyclic vein formation and deformation

The homogenous domain appears as an asymmetrical alteration selvedge with metasomatism so intense that there has been complete destruction of the original mineralogy and extreme bulk compositional change. The diffuse zone of manganese enrichment at the boundary between the two regions is consistent with the homogenous domain being the alteration selvedge to the vein, which grades into the pseudomorphed domain. However, the difference in immobile trace elements (e.g. titanium, zirconium, Fig. 4b) between the two domains is not consistent with derivation from the same protolith. We suggest instead that the homogenous domain is an older vein that has been recrystallized and fractured by the later quartz vein. Elements conventionally considered immobile (e.g. titanium, zirconium) are present in the pseudomorphed domain, but are absent from the homogenous domain. This demonstrates that the homogenous domain was originally a different composition from the pseudomorphed domain. The presence of the titanium-bearing grains within the zone of diffuse manganese enrichment also shows that this zone was originally part of the homogenous domain that has minor amounts of manganese-rich vein material in it. Observations made at the outcrop scale that veins are often re-fractured during subsequent fluid pressure cycles are consistent with the homogenous domain being a previously deformed vein.

The lack of CPO indicates that deformation was not predominantly by dislocation creep. However, the dolomite component of the homogenous domain has a patchy CPO, where spatially clustered grain aggregates exhibit similar orientations. Patchy CPOs have been previously observed in dolomite where neoblasts inherited the orientation of their parent grain with limited subsequent rotation (Leiss & Barber 1999). This phenomenon has also been observed in albite where it is due to chemically driven neocrystallization during deformation by granular flow and the CPOs are unrelated to the bulk deformation kinematics (Jiang *et al.* 2000). Similarly, if the rocks deformed by fracturing, but with little subsequent shearing and further comminution, adjacent grains would share orientations. The quartz does not appear to show the same patchy CPO as the dolomite, even within the almost monomineralic quartz domain.

Under the conditions of ore body formation at SDGM (>300°C and 1–3 kbar; Baker *et al.* 2010), dolomite would be expected to deform by brittle fracture. However, examples of natural dolomite fault rocks show evidence of the onset of recrystallization at lower temperatures (*c.* 270°C) where fluids are present (Newman & Mitra 1994), possibly due to chemically driven neocrystallization and not driven by strain alone. The patchy CPOs present in this sample and the overall lack of a CPO are consistent with a combination of one or more of chemically driven recrystallization and brittle fracturing in a low strain environment. The phase mixing in the quartz–dolomite part of the microstructure would have occurred at this time by the precipitation of quartz at triple junctions and along micro-fractures, in a similar way to the processes outlined by Kruse & Stünitz (1999) and Kenkmann & Dresen (2002).

Comparison between experimental and natural quartz samples (Hirth & Tullis 1994) suggest that the quartz would be in a semi-brittle deformational regime with limited dislocation mobility. The generation of a random CPO by brittle processes probably requires larger strains than the patchy CPO in the dolomite would allow. Therefore it is suggested that the quartz-rich domain may be deforming by brittle fracture, whereas the dolomite-rich region is undergoing chemically driven recrystallization and quartz precipitation. These microstructures show that, although chemically homogenous at the scale of the synchrotron XFM maps, this region contains a wealth of information about how rocks deform in mineral deposits and how successive generations of first dolomite, then quartz, then calcite veins overprint one another both physically and chemically.

Relationship between sulphide and gold mineralization

The coarse-grained pyrites within the barren zone are growing around a thin quartz vein (c-py in Fig. 6c), consistent with this being a locus of fluid flow. During fluid flow the bulk composition of the rocks can change significantly with the introduction of some elements (including gold and arsenic) and the removal of others. The arsenic is present within both the coarse and fine-grained pyrite (f-py in Fig. 6c) populations, indicating that these were growing during fluid flow. The barren zone could either be a vein of a different composition to the rest of the rock (as highlighted in the previous section), a zone of coarse pyrite growth, or a zone of coarsening following the initial growth of fine-grained pyrite.

A uniform distribution of titanium-bearing grains across the barren zone (Fig. 6f) shows that

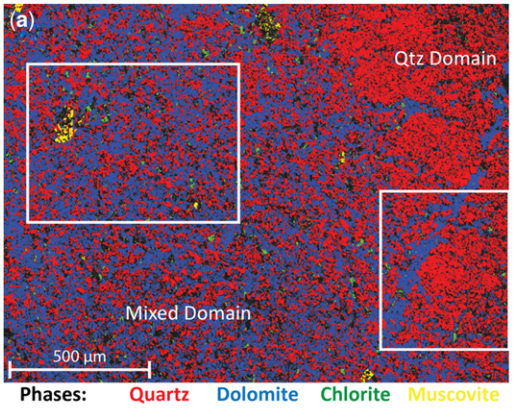

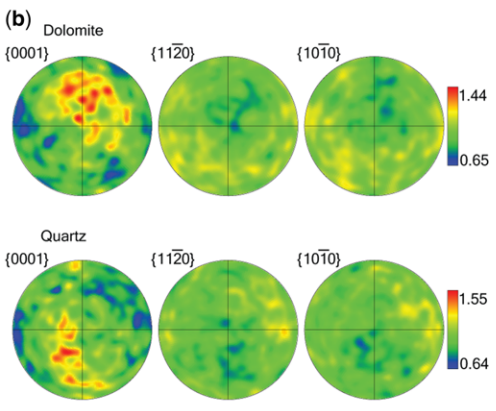

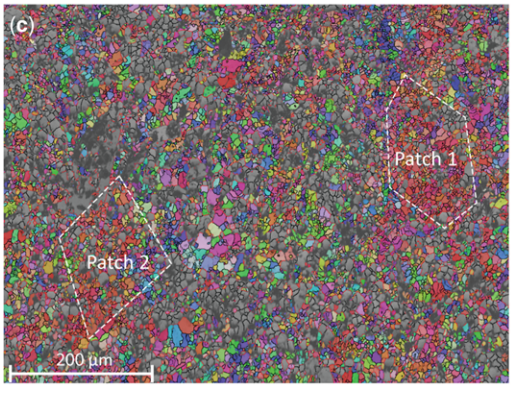

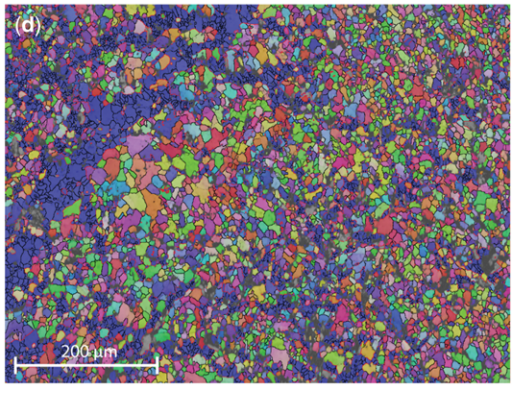

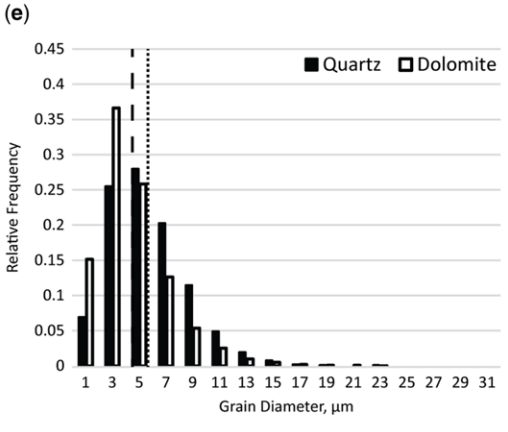

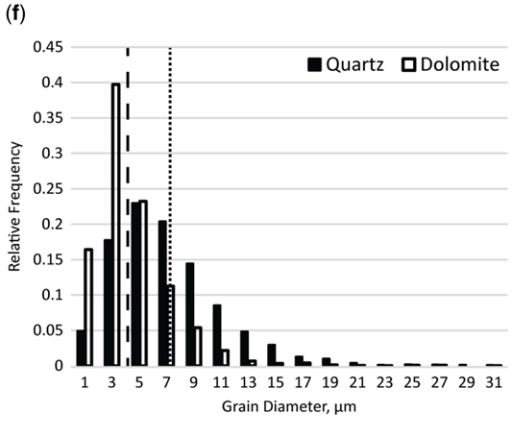

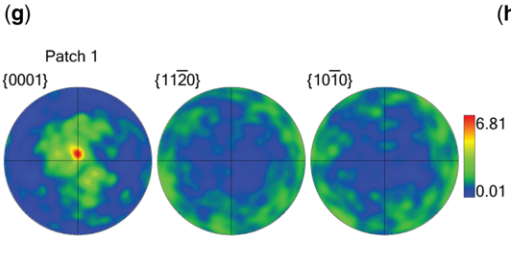

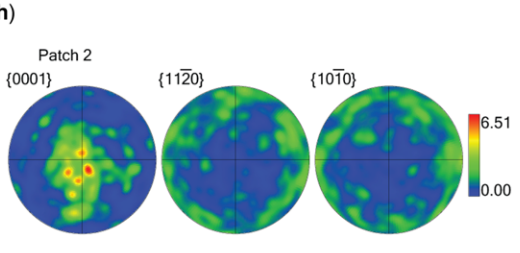

it is not vein material, but has the same composition as the rest of the rock, although with no fine-grained pyrite. Rough bulk composition calculations from areal sums of the synchrotron datasets show that the regions surrounding the barren zone have similar Rb/Sr and Ti/Zr ratios (i.e. these elements are immobile). Iron varies between 8 and 13% and, with the exceptions of the barren zone, the Fe/As ratios are consistent (*c.* 65). The barren zone is lower in arsenic (Fe/As = 214). This suggests that the coarse sulphide occurred separately to the fine-grained sulphide and is not just a product of post-pyrite growth coarsening in a closed system. The coarse zones are associated in three dimensions with increased gold concentration (Fig. 7) due to protracted fluid flow that led both to the addition of gold and the growth of the coarse sulphides.

As the chemical zoning developed in the pyrites records the mineral growth and has not been modified post-deposition, this zoning records the hydrothermal fluid flow in the deposit. High arsenic concentrations occur as several growth zones within the coarse-grained pyrites. The geometry of these zones is slightly cryptic in some pyrites, but clearly forms two parallel growth bands in others. The same compositional range encompasses the majority of the fine-grained pyrite. Oscillatory zoning in minerals can be attributed to oscillations in pressure, temperature and bulk composition driven by externally derived disequlibrium fluids (Ord *et al.* 2012) or local kinetically controlled fractionation that develops due to differences in mineral growth rates and inter-crystalline diffusion (Shore & Fowler 1996). Recent models of non-hydrostatic metamorphism suggest that the grain-scale stress distribution may also be able to control the composition of minerals precipitated (Wheeler 2014). Given the variations in stresses that can be inferred from repeated veining, the effect of non-hydrostatic equilibrium should also be kept in mind. It is not possible to say unequivocally which of these is the driving force for the observed zoning, but we postulate that the coarse pyrites began growing in an arsenic-absent environment and continued to grow, along with the finer grained pyrite, during or after the addition of arsenic to the rock over a length scale >10 cm. It is likely that the first-formed pyrite is coarse due to growth proceeding faster than nucleation, possible in the open space of the forming quartz vein in which they sit. Sulphur was introduced by the fluid and iron was consumed from around the growing pyrites by the breakdown of chlorite to sericite, forming an iron-depleted zone around the pyrites similar to the aluminium depletion zones that have been shown to develop around garnet porphyroblasts when growth is diffusion-limited (Carlson 1989). The fluid distribution was subsequently more uniform through the rocks and nucleation was easier, possibly due to higher degrees of supersaturation or the presence of arsenic. The low iron concentration around the coarse pyrites prevented further nucleation.

Microscale constraints on macroscopic processes at SDGM

Sulphide microstructures and chemical zoning point to evolving fluid compositions during alteration by dissolution and re-precipitation. The pyrite zoning (Fig. 6c) shows that coarse-grained pyrite begins to grow in an arsenic-poor environment. As they grow, consuming sulphur that enters the rock locally along the fracture that they sit along, they remove the iron from the surrounding rock by the breakdown of chlorite to produce pyrite. If the growth is limited by the availability of sulphur, the rock is never significantly supersaturated with respect to pyrite, retarding the nucleation of new grains. The removal of iron and the breakdown of chlorite increases the wall rock permeability, allowing wider alteration zones. Evolution of the fluid composition to be more arsenic-rich with a higher sulphur activity leads to large-scale growth of the

Fig. 5. Electron back-scattered diffraction data showing microstructure of homogenous domain adjacent to quartz vein in Figure 4. (**a**) Phase map showing monomineralic quartz and quartz–dolomite areas. Dataset consists of a map of 1800 × 1475 pixels and has a step size of 1 μm collected overnight. Chlorite is distributed through the matrix and muscovite forms porphyroblasts. White boxes show locations of detailed datasets in (c) and (d). (**b**) Contoured pole figures of dolomite fabrics contoured using a cone with a 10° half-width. Values denote multiples of a mean uniform distribution. Values close to unity show that there is no preferred orientation within either phase. (**c**) Orientation map of dolomite in the polymineralic domain using an inverse pole figure colour scheme relative to sample surface normal (*z*). Patches denote manually identified areas of similar orientation selected for analysis in (g) and (h). (**d**) Orientation map of quartz in the monomineralic domain using an inverse pole figure colour scheme relative to sample surface normal (*z*). Dolomite is coloured blue. (**e**) Grain size distribution for the polymineralic domain. Dashed lines show mean grain size for each phase. (**f**) Grain size distribution for the monomineralic domain. Dashed lines show mean grain size for each phase. (**g**) Contoured pole figures of dolomite fabrics from within patch 1 (in a) contoured using a cone with a 10° half-width. Values denote multiples of a mean uniform distribution. (**h**) Contoured pole figures of dolomite fabrics from within patch 2 (in c) contoured using a cone with a 10° half-width. Values denote multiples of a mean uniform distribution.

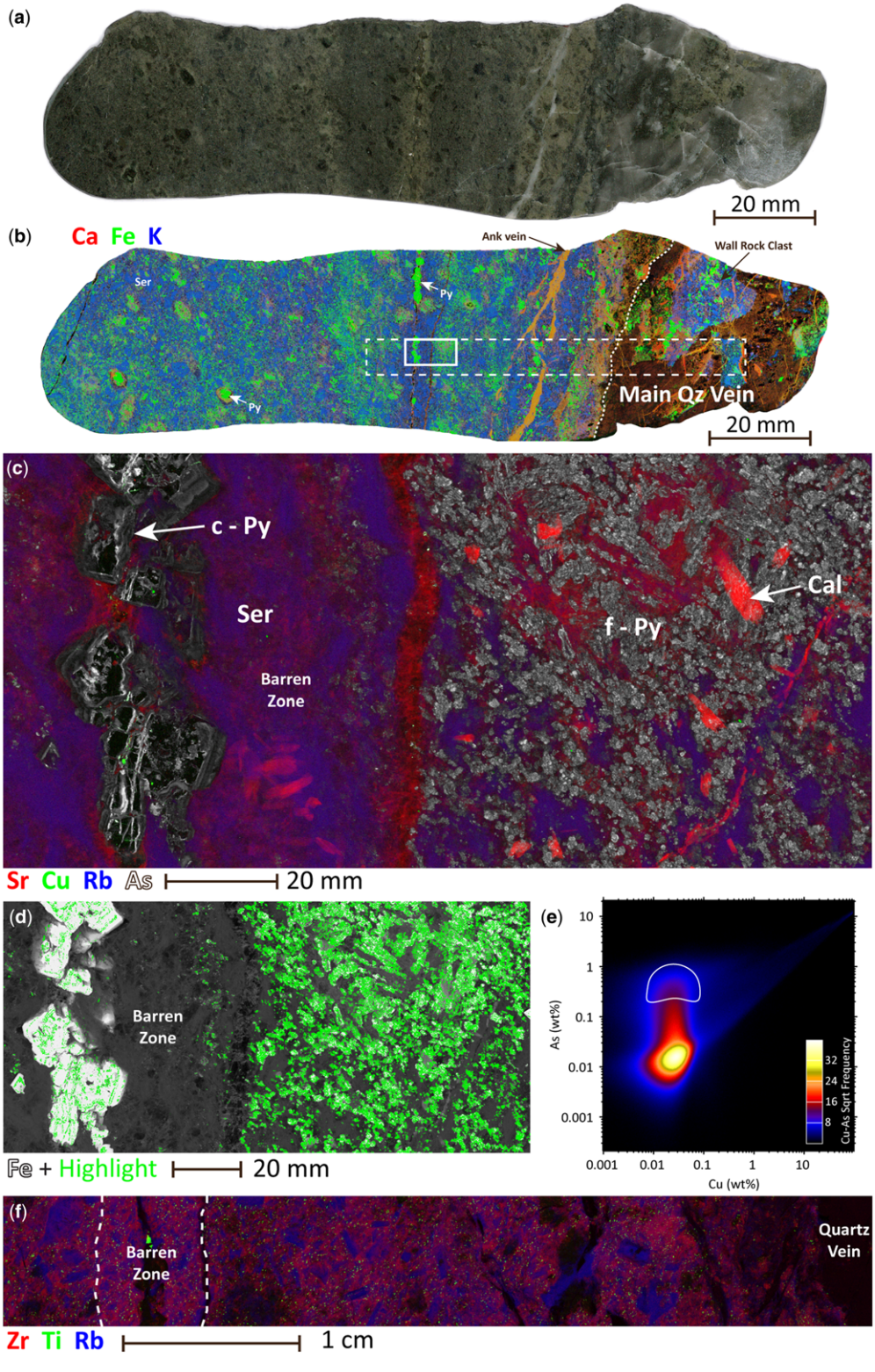

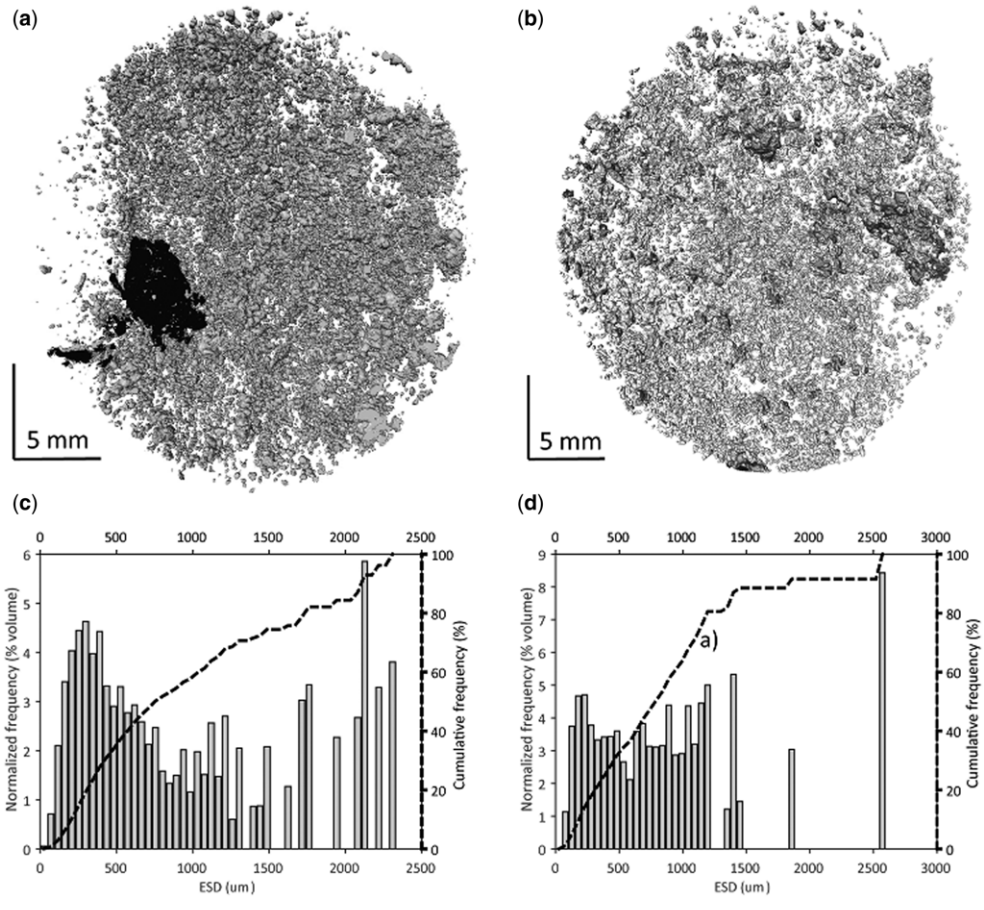

Fig. 7. High-resolution X-ray computed tomography data showing sulphide (grey) and gold (black) distribution from two 25 mm sub-sample cores of sample GQ3. (**a**) Rendering of particles in a native gold-bearing sub-sample. (**b**) Rendering of particles in a barren sub-sample from *c.* 10 cm away from (a). (**c**, **d**) Crystal size distributions for each dataset are shown as equivalent spherical diameter of the particles. The cumulative frequency curves are also shown (dashed line). The frequency plots show a decrease in the frequency of particles between 600 and 1200 μm and an increase in frequency of particles coarser than 1200 μm, indicating a coarsening of particles close to the gold mineralization.

Fig. 6. Chemical analysis of sample GQ3. (**a**) Optical image of the analysed rock slab. Bleached zones show alteration around veins and the main vein on the right-hand side cuts across wall rock clasts. (**b**) Red–green–blue composite map of microscale X-ray fluorescence data with calcium (red), iron (green) and potassium (blue) showing the entire sample mapped at a 25 μm pixel size. Pyrite (green) is distributed throughout the sericitized (blue) wall rock, including in wall rock pieces within the gold-bearing quartz vein (darker area on the right-hand side). Dolomite/ankerite (ank) veins are spatially coincident with the quartz vein. White dashed box shows the extent of the synchrotron XFM map. Solid white box shows part of XFM map shown in (b) and (c). (**c**) Red–green–blue composite image of XFM data showing strontium (red), copper (green) and rubidium (blue). This is superimposed on arsenic variations (greyscale from black = 0 to white = max) within the pyrite. Map produced from a dataset of 32.7 megapixels collected in about nine hours with a step size of 4 μm, a dwell time of 0.98 ms/pixel (full dataset shown in (f)). (**d**) Iron intensity map (greyscale) with compositions of pyrite outlined in (e) highlighted. The two scales of pyrite, coarse and fine grained, are denoted by c-py and f-py, respectively. (**e**) Composition plot of arsenic versus copper contoured for data density. White outline shows compositions highlighted in (c). (**f**) Red–green–blue composite map showing zircon (red), titanium (green) and rubidium (blue) across the entire alteration zone to the quartz vein. Titanium is uniformly distributed across the barren zone, indicating that this is all the same lithology as the zones containing the fine-grained pyrite.

fine-grained pyrite throughout the alteration halo. Potentially superimposed on this are the effects of local equilibrium, kinetic fractionation due to the limited diffusion length scale and non-hydrostatic stresses.

The data presented here are consistent with previous studies (Blenkinsop *et al.* 2007; Hantler 2009; Baker *et al.* 2010; Oliver *et al.* 2012) that showed multiple vein-forming deformation events that are spatially localized such that the same rocks are fractured in each event, although the absolute timescale is not constrained. Distal alteration across one alteration halo in the GQ lode is limited to pseudomorphing of the original igneous microstructure by a calcite–sericite–chlorite assemblage (Fig. 3). Despite the high mica content, which often leads to weakening, these rocks remain relatively unsheared. Closer to the gold-bearing quartz veins, the dolomite veins show evidence for a combination of chemically driven recrystallization and brittle deformation (Fig. 5). Since the initial dolomitization, the rocks have been fractured with several generations of quartz, dolomite and calcite veins. None of these microstructures show significant evidence for major shear strain, with only minor centimetre-scale offset on any fractures in the outcrop (Fig. 2). This style of deformation can be generated by repeated cycles of fluid pressure building up and releasing during brecciation, as hypothesized by Baker *et al.* (2010) based on data from fluid inclusion studies. Cycles of pressure release and fluid flow lead to large integrated fluid fluxes through the rocks. In contrast with some modestly sized deposits where small fluid volumes have been inferred based on the extent of alteration (Pearce *et al.* 2015), SDGM was the focus of protracted fluid flow with temporally varying compositions. Moreover, the gold mineralization is spatially associated with the fluid flow loci highlighted by coarse-grained pyrite in the HRXCT datasets. The lack of appreciable deformation within any of the alteration zones is due to much of the deformation being brecciation caused by elevated fluid pressure (Cox 2010) rather than due to high differential stresses that would cause shearing.

Case study 2: compositional and microstructural variations in sulphide ores from Mt Keith, Western Australia

Geological background

The Mt Keith nickel sulphide deposit is located in the Wiluna Domain of the Kalgoorlie Terrane of the Yilgarn Craton, Western Australia (Hill & Gole 1990). The Agnew Wiluna Greenstone Belt (*c.* 2·7 Ga in age) consists of felsic to intermediate volcanic and volcaniclastic rocks and sedimentary rocks (mainly composed of sulphidic cherts and carbonaceous shales) with komatiites and komatiitic basalts. The belt contains several world-class nickel sulphide deposits and is considered to be the most nickel-endowed region in the world after the major Sudbury and Noril'sk-Talnakh camps (Hronsky & Schodde 2006). The Mt Keith (referred to as the MKD5) deposit represents the world's largest accumulation of komatiite-associated magmatic sulphide and is one of the best example of low-grade, low-tonnage type II nickel sulphide hosted in komatiite (Grguric *et al.* 2006). The deposit is hosted in the Mt Keith Ultramafic Unit, which is formed by olivine adcumulates (dunites) flanked laterally by olivine meso- to orthocumulates (Rosengren *et al.* 2005; Grguric *et al.* 2006; Rosengren *et al.* 2008). The primary igneous silicate minerals in these rocks have been completely replaced by secondary minerals; however, there is an excellent pseudomorphic preservation of the igneous textures. Most of the economic mineralization is characterized by S/Ni ratios >1 and a sulphide abundance varying between 0.5 and 5 vol%. The sulphide minerals present consist mainly of pentlandite and pyrrhotite and result from the crystallization of a magmatic sulphide liquid. Sulphide liquids crystallize as a mono-sulphide solid solution and an intermediate solid solution and subsequently unmix to form polymineralic aggregates, typically of pentlandite, pyrrhotite and chalcopyrite with variable, but minor, amounts of pyrite.

The PGEs (including platinum, palladium, osmium, iridium, ruthenium and rhodium) and semi-metals (e.g. selenium, arsenic, bismuth and tellurium) have large partition coefficients with respect to sulphide (see reviews by Barnes & Lightfoot 2005; Mungall & Brenan 2014). Consequently, as soon as a sulphide liquid forms, it will collect the PGEs and semi-metals from the coexisting silicate magma. The metal concentrations in the sulphide (relative to those in the parent magma) are mainly a function of two parameters: the relative masses of the silicate magma and the sulphide liquid (Campbell & Naldrett 1979) and the kinetics of PGE diffusion through the boundary layers around sulphide liquid droplets (the kinetic factor; Mungall 2002). PGEs behave as immobile elements during the alteration or metamorphism of disseminated sulphide hosted in komatiites (Barnes & Liu 2012). As a result, the PGE and semi-metal concentrations in sulphide minerals may be used as a fingerprint of silicate magma–sulphide liquid interactions. Previous LA-ICP-MS studies on the distribution of PGEs and other trace elements (including selenium, arsenic, bismuth, tellurium and cobalt) within magmatic base–metal sulphides have focused on sulphides from PGE and nickel–PGE sulphide deposits hosted in mafic intrusions, with only a

few studies carried out on sulphides associated with komatiites.

Recent HRXCT studies have highlighted the presence of four main sulphide textures and sulphide distributions at Mt Keith, based on the abundance, the 3D size, the morphology, the degree of connectivity and the distribution of the sulphide minerals (Godel 2013; Godel *et al.* 2013). In this case study we use this classification, along with the variations in trace element concentrations from the LA-ICP-MS mapping of sulphides, to constrain large-scale sulphide–silicate melt interactions during komatiite-hosted magmatic sulphide ore formation.

Analytical techniques applied to Mt Keith samples

Samples of different ore types from the Mt Keith nickel sulphide deposit were scanned using an XRADIA XRM 500 3D X-ray microscope. The acquisition parameters and details of data processing are given in Godel *et al.* (2013). Trace element concentrations for selected elements were measured using a Thermo X7 ICP-MS system coupled with a New Wave Research 213 nm Nd:YAG UV laser ablation system in the raster mode.

Results

The main textures of sulphides observed by Godel *et al.* (2013) are shown in Figure 8: (1) finely disseminated sulphides (Fig. 8a); (2) disseminated to slightly interconnected sulphides (Fig. 8b); (3) disseminated to globular sulphides (Fig. 8c); and (4) disseminated to strongly interconnected sulphides. The finely disseminated sulphides (Fig. 8a) are characterized by the presence of sub-spherical (sphericity >0.98) sulphide aggregates that are homogeneously distributed within the samples (up to *c.* 1.5 vol% sulphide). These small sulphide aggregates are located at the olivine crystal boundaries and more particularly at the olivine triple junctions. The sulphide aggregates have a size ranging from a few tens of micrometres to *c.* 1000 μm equivalent sphere diameter (Fig. 9). In contrast with the finely disseminated sulphides, all other sulphide distributions are characterized by the presence of a multimodal population of sulphide aggregates (Figs 8b, c & 9). The size and degree of connectivity of the sulphides increase drastically in the samples with sulphide abundance >1.5 vol%. In such cases, a large proportion of the sulphides form networks of variable size. The sulphide topology in these samples is controlled by the olivine crystal boundaries and is inherited from the morphology of idiomorphic olivine crystals with 3D dihedral angles around 125° (Godel 2013). The extent of the sulphide networks is strongly correlated with the sulphide proportions, with the largest interconnected network forming locally up to 20 vol% of the rocks and up to 95% of the sulphide forming a single interconnected network.

The combination of HRXCT with LA-ICP-MS mapping and analysis (Fig. 8 and Godel *et al.* 2013) reveals the behaviour of the PGEs and other trace elements (including selenium, arsenic, bismuth and tellurium) at the sulphide aggregate scales (Fig. 8d–g) and in pentlandite and pyrrhotite in particular. At Mt Keith, platinum, iridium and gold are below the detection limits in the bulk sulphides, but form distinct small (a few micrometres in diameter) minerals (mainly sperrylite and irarsite). This behaviour is similar to that observed in other nickel–copper–PGE sulphide deposits (for a reveiw, see Godel 2015). Ruthenium, rhodium and osmium are strongly correlated with variations in arsenic and tellurium concentrations within pentlandite (Fig. 8g). Palladium, selenium and cobalt are the only elements whose concentration remains relatively constant within either pentlandite or pyrrhotite at the sulphide aggregate scale (Fig. 8g), with concentrations usually an order of magnitude higher in pentlandite than in pyrrhotite.

Magma dynamics of komatiite-hosted nickel sulphide deposits

The textures of sulphide ores described here result from interactions between sulphide and silicate melts prior to and during emplacement of the ore bodies. The trace element compositions of the sulphide minerals can be used to infer the extent of any interactions between the two melt phases. Cobalt has a low partition coefficient between sulphide and silicate liquids and is relatively mobile on the microscale in a large range of environments and has been shown to be erratic at Mt Keith (Gole 2014). Similarly, selenium has a relatively low (*c.* 1000) partition coefficient between sulphide and silicate liquids compared with palladium (*c.* 1 000 000) and hence cobalt and selenium are expected to be less sensitive in monitoring sulphide–silicate liquid interactions. This is consistent with the relatively low and constant selenium concentrations recorded for the different sulphide textures at Mt Keith (Godel *et al.* 2013). By contrast, the palladium concentrations in pentlandite vary by an order of magnitude (from *c.* 1 to 10 ppm) within and between samples. Comparison of palladium concentrations in pentlandite and the 3D size of the corresponding sulphide aggregates reveals a strong correlation between the two (Godel *et al.* 2013). Comparison of the average palladium concentrations in pentlandite from samples exhibiting different sulphide distributions and topology (Fig. 8d–f) highlight the fact that samples

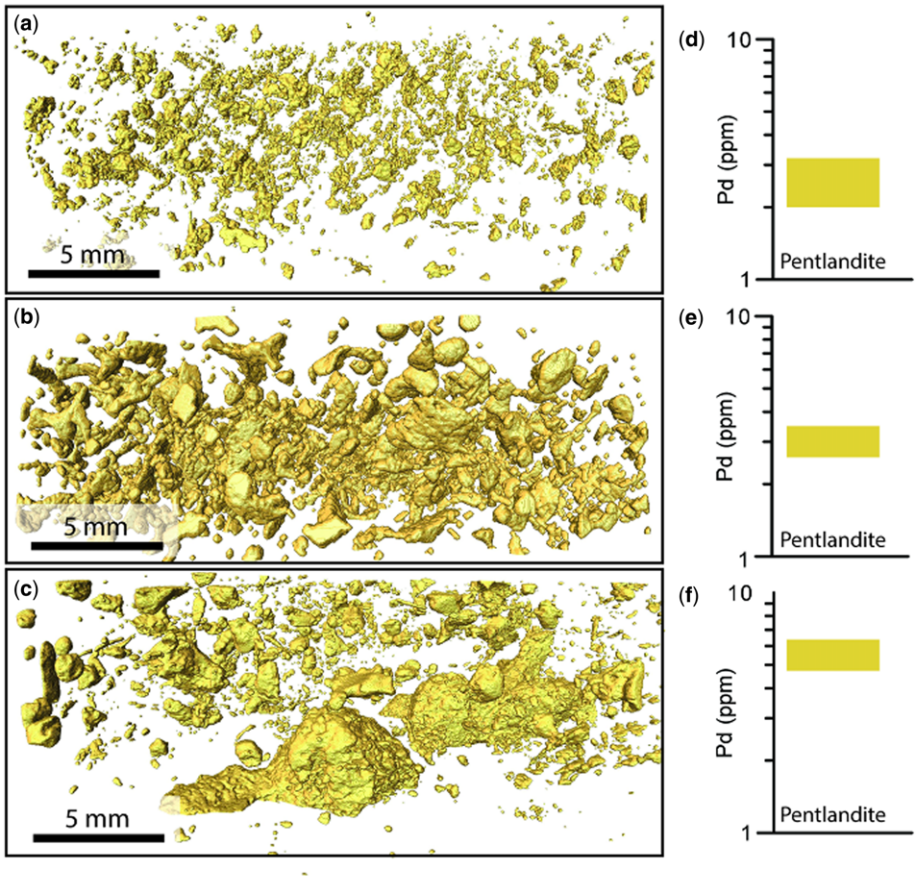

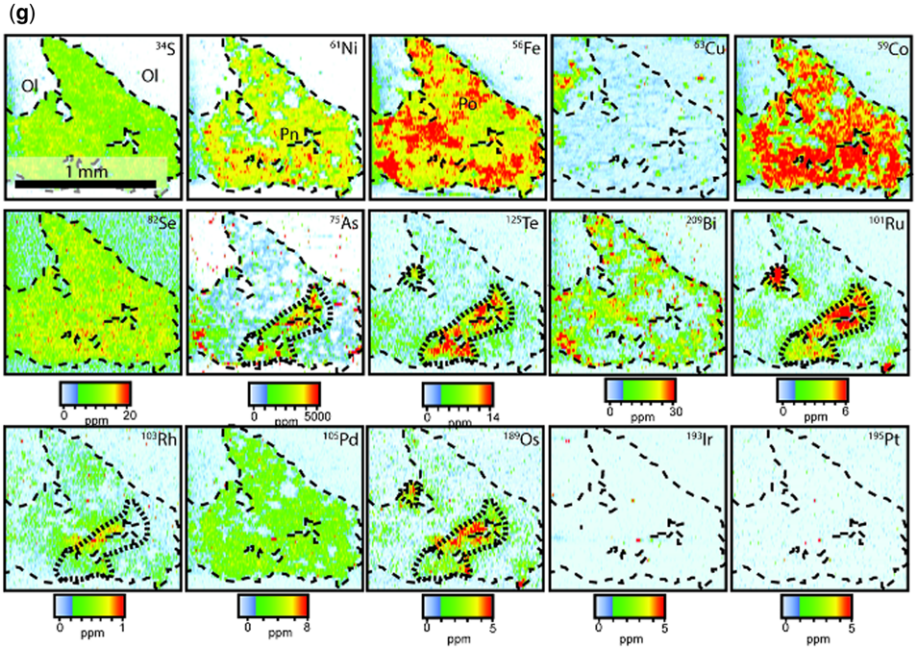

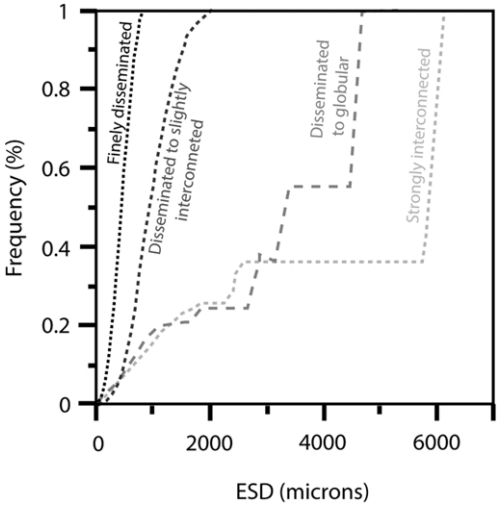

Fig. 9. Size distribution of sulphide aggregates in samples from Mt Keith exhibiting a range of sulphide textures. The data are presented as normalized volume frequency (i.e. total volume of sulphide within a bin range divided by the total volume of sulphide in the sample) as a function of equivalent sphere diameter (ESD) range.

containing globular sulphides (Fig. 8c) have higher average palladium concentrations in pentlandite. This is interpreted to reflect the greater interaction of the larger sulphide aggregates with silicate magma during transport in the flowing magma compared with smaller sulphide aggregates that formed by *in situ* nucleation with minimal transport (Godel *et al.* 2013). In addition, the samples that contain a higher proportion of large globular sulphides (up to a few centimetres in diameter, easily recognizable in drillcore) also have a higher grade of nickel. As such, these sulphide morphologies are important during an exploration/logging campaign to quickly define the potential of the system to transport and deposit higher grade sulphide-rich ores or to locate areas of higher metal grade (Godel 2013; Godel *et al.* 2013; Robertson *et al.* 2015) providing that a large number of samples are analysed.

The data presented here show that the relatively uniform palladium compositions within pentlandite grains from the Mt Keith deposit result from large-scale interactions between the silicate and sulphide melts. The interaction results in the enrichment of palladium and the formation of large sulphide globules. This coupled analysis of the 3D sulphide distribution, size and morphology by HRXCT with *in situ* measurements of the palladium concentrations in pentlandite using LA-ICP-MS not only allows an insight into the dynamics of the magmatic system and the formation of the ore, but also support the generation of new exploration models to better target higher grade nickel ores. Current technological developments allow the acquisition and processing of a large number (hundreds) of samples with the capacity steadily increasing. As such, this workflow can easily be translated into practical use during an exploration campaign.

Microscale to mineral system: scale integration of datasets over 10 orders of magnitude

Microanalysis coupled with higher resolution nanoscale techniques, such as atom probe tomography and NanoSIMS, allows the atomic- to core-scale analysis of mineral chemistry and microstructures. Although these scales of data are key to understanding the processes that form mineral deposits, alteration halos and other 'distal footprints', they are relatively time consuming and expensive, which leads to questions of how representative the analyses are of the system. Therefore it is essential to integrate microanalyses within the larger deposit-scale datasets that are routinely collected during exploration and mining. Portable XRF measurements and hyperspectral core mapping have been used successfully to define both lithostratigraphy (Gazley *et al.* 2011; Haest *et al.* 2012) and alteration (Mauger *et al.* 2007; Roache *et al.* 2011; Yuan *et al.* 2014) in and around ore deposits. However, although semi-automated systems are quantitative and objective, the discrepancies that have arisen during testing suggest that further verification may always be necessary (Mauger & Hore 2009). To gain full advantage from a truly multiscale analysis, datasets should be linked together spatially so that, where possible, the more detailed analyses are carried out on representative parts of the system that refine our understanding of the microstructures and,

Fig. 8. Three-dimensional distribution of sulphides in samples from Mt Keith exhibiting three different sulphide textures: (**a**) finely disseminated sulphides; (**b**) finely disseminated to interconnected sulphide network; and (**c**) finely disseminated to globular sulphide. The average palladium concentrations in pentlandite analysed from a range of three-dimensional size and morphology of the sulphides in these samples are presented in (**d**), (**e**) and (**f**). (**g**) Example of laser ablation inductively coupled plasma mass spectrometry map of a disseminated sulphide aggregate from (b) showing the variable behaviour of platinum group elements and semi-metals at the sulphide aggregate scale (see text for further explanation).

ultimately, processes inferred from larger scale analysis. For example, drillcore may be domain-based on visual logging, picoscale XRF logging or hyperspectral mapping and the domains that exhibit interesting gradients in chemistry or are of high grade may be sent for microscale XRF mapping. The key reactions or host phases can subsequently be investigated using detailed SEM-based analysis. If mineral replacement or deformation is important, EBSD may be able to guide the interpretation by linking the reactants and products or investigating deformation mechanisms to constrain temperature and stress conditions. The impact of key processes (replacement, deformation, ore mineral precipitation) on the trace element content can be quantified using LA-ICP-MS or PIXE mapping to record temporal variations through, for example, zoned minerals. The preceding workflow relies on the analyses being carried out in an appropriate order, with the least destructive and most sensitive analyses (e.g. CL) being performed before the analyses that have the potential to cause minor lattice defects (e.g. PIXE or EBSD on sensitive phases) or to remove material (e.g. LA-ICP-MS). Once the microscale processes are understood, an important and often overlooked step is to upscale our microscale understanding of these processes to inform both the large-scale processes (e.g. the repeated cycling of fluid flow and brecciation in the absence of large-scale shearing) and the signatures that can aid exploration – for example, the breakdown of iron-bearing mica enhancing permeability during metasomatism and thus localizing fluid flow and the subsequent gold mineralization that is manifested in hyperspectral core-scale or satellite-derived datasets. The process-driven approach to exploration should ultimately lead to a set of selection criteria for whether a particular exploration model is applicable. This will make model selection more robust than if using only empirical relationships (e.g. gold correlates with arsenic).

Compilations of chemical and mineralogical logs into 3D models allows the architecture of deposit to camp-scale plumbing systems to be understood (Fisher *et al.* 2013; Hill *et al.* 2014*a*) and statistically robust spatial associations to be defined between the commodity of interest, the particular pathfinder elements or minerals (Hill *et al.* 2014*b*) and phases of deformation. To understand fully the processes active during deposit formation, these phenomenological associations should be tested at the microscale to identify their exact role in ore genesis. We have shown here that, once established, the locus of fluid flow and alteration is concentrated via repeated cycles of pressure build-up and release. This can lead to protracted and complex alteration halos that are impossible to deconvolve using core-scale observations. For example, the co-location of gold with sulphide, carbonate and potassic alteration is common in greenstone-hosted gold, with gold mineralization often linked to sulphide precipitation. However, it has recently been shown that, at the microscale, gold is intimately associated with reactions between carbonate and potassium-bearing minerals and not with sulphides (Pearce *et al.* 2015).

As microscale techniques become increasingly widely used, it is likely that the results will drive an ongoing reassessment of many established models for ore genesis, with changes in the weighting given to microscale and macroscale features in localizing ore deposition.

This research was undertaken on the X-ray fluorescence microscopy beamline at the Australian Synchrotron, Victoria, Australia and was funded by AngloGold Ashanti. LS acknowledges support from a CSIRO Mineral Resources Flagship Internship to support this work. Steve Reddy is thanked for assistance with collecting the large-area EBSD data used in this study. The LA-ICP-MS data were collected at the Earth Materials Laboratory at the Université du Québec à Chicoutimi. We thank Sandra Piazolo and an anonymous reviewer for improving the structure and clarity of our 'ambitious' paper.

References

Baker, T., Ebert, S., Rombach, C. & Ryan, C.G. 2006. Chemical compositions of fluid inclusions in intrusion-related gold systems, Alaska and Yukon, using PIXE microanalysis. *Economic Geology*, **101**, 311–327, https://doi.org/10.2113/gsecongeo.101.2.311

Baker, T., Mustard, R. *et al.* 2008. Mixed messages in iron oxide-copper-gold systems of the Cloncurry district, Australia: insights from PIXE analysis of halogens and copper in fluid inclusions. *Mineralium Deposita*, **43**, 599–608, https://doi.org/10.1007/s00126-008-0198-y

Baker, T., Bertelli, M., Blenkinsop, T., Cleverley, J.S., McLellan, J., Nugus, M. & Gillen, D. 2010. P-T-X conditions of fluids in the Sunrise Dam Gold Deposit, Western Australia, and implications for the interplay between deformation and fluids. *Economic Geology*, **105**, 873–894, https://doi.org/10.2113/econgeo.105.5.873

Barker, S.L.L., Hickey, K.A., Cline, J.S., Dipple, G.M., Kilburn, M.R., Vaughan, J.R. & Longo, A.A. 2009. Uncloaking invisible gold: use of nanoSIMS to evaluate gold, trace elements, and sulfur isotopes in pyrite from Carlin-type gold deposits. *Economic Geology*, **104**, 897–904, https://doi.org/10.2113/econgeo.104.7.897

Barnes, S.J. & Liu, W. 2012. Pt and Pd mobility in hydrothermal fluids: evidence from komatiites and from thermodynamic modelling. *Ore Geology Reviews*, **44**, 49–58, https://doi.org/10.1016/j.oregeorev.2011.08.004

Barnes, S.J., Fiorentini, M.L., Austin, P., Gessner, K., Hough, R. & Squelch, A.P. 2008. Three-dimensional morphology of magmatic sulfides sheds light on ore

formation and sulfide melt migration. *Geology*, **36**, 655–658.

Barnes, S.J., Wells, M.A. & Verrall, M.R. 2009. Effects of magmatic processes, serpentinization, and talc-carbonate alteration on sulfide mineralogy and ore textures in the Black Swan disseminated nickel sulfide deposit, Yilgarn Craton. *Economic Geology*, **104**, 539–562, https://doi.org/10.2113/gsecongeo.104.4.539

Barnes, S.J., Godel, B.M., Locmelis, M., Fiorentini, M.L. & Ryan, C.G. 2011. Extremely Ni-rich Fe-Ni sulfide assemblages in komatiitic dunite at Betheno, Western Australia: results from synchrotron X-ray fluorescence mapping. *Australian Journal of Earth Sciences*, **58**, 691–709, https://doi.org/10.1080/08120099.2011.586048

Barnes, S.J., Fisher, L.A. *et al.* 2016. Primary cumulus platinum minerals in the Monts de Cristal Complex, Gabon: magmatic microenvironments inferred from high-definition X-ray fluorescence microscopy. *Contributions to Mineralogy and Petrology*, **171**, 1–18, https://doi.org/10.1007/s00410-016-1232-1

Barnes, S.-J. & Lightfoot, P.C. 2005. Formation of magmatic nickel-sulfide ore deposits and processes affecting their copper and platinum-group element contents. *In*: Hedenquist, J.W., Thompson, J.F.H., Goldfarb, R.G. & Richards, J.P. (eds) *Economic Geology 100th Anniversary Volume*, Society of Economic Geologists, Littleton, CO, 179–213.

Barnes, S.-J., Cox, R. & Zientek, M. 2006. Platinum-group element, gold, silver and base metal distribution in compositionally zoned sulfide droplets from the Medvezky Creek Mine, Noril'sk, Russia. *Contributions to Mineralogy and Petrology*, **152**, 187–200.

Barrie, C.D., Boyle, A.P. & Prior, D.J. 2007. An analysis of the microstructures developed in experimentally deformed polycrystalline pyrite and minor sulphide phases using electron backscatter diffraction. *Journal of Structural Geology*, **29**, 1494–1511, https://doi.org/10.1016/j.jsg.2007.05.005

Barrie, C.D., Boyle, A.P., Cox, S.F. & Prior, D.J. 2008. Slip systems and critical resolved shear stress in pyrite: an electron back-scatter diffraction (EBSD) investigation. *Mineralogical Magazine*, **72**, 1181–1199, https://doi.org/10.1180/minmag.2008.072.6.1181

Blenkinsop, T., Baker, T., McLellan, J., Cleverley, J. & Nugus, M. 2007. *Sunrise Dam Gold Mine, Project G15, Final Report*. Predictive Mineral Discovery Cooperative Research Centre, Geoscience Australia online, Geoscience Australia Catalogue 69793.

Brown, S.M., Johnson, C.A., Watling, R.J. & Premo, W.R. 2003. Constraints on the composition of ore fluids and implications for mineralising events at the Cleo gold deposit, Eastern Goldfields Province, Western Australia. *Australian Journal of Earth Sciences*, **50**, 19–38.

Brugger, J., Pring, A. *et al.* 2010. Probing ore deposits formation: new insights and challenges from synchrotron and neutron studies. *Radiation Physics and Chemistry*, **79**, 151–161, https://doi.org/10.1016/j.radphyschem.2009.03.071

Bunton, J., Lenz, D., Olson, J., Thompson, K., Ulfig, R., Larson, D. & Kelly, T. 2006. Instrumentation developments in atom probe tomography: applications in semiconductor research. *Microscopy and Microanalysis*, **12**, 1730–1731, https://doi.org/10.1017/S1431927606065809

Campbell, I.H. & Naldrett, A.J. 1979. The influence of silicate: sulphide ratios on the geochemistry of magmatic sulphides. *Economic Geology*, **74**, 1503–1505.

Campbell, S.G., Reith, F., Etschmann, B., Brugger, J., Martinez-Criado, G., Gordon, R.A. & Southam, G. 2015. Surface transformations of platinum grains from Fifield, New South Wales, Australia. *American Mineralogist*, **100**, 1236–1243, https://doi.org/10.2138/am-2015-4905

Carlson, W.D. 1989. The significance of intergranular diffusion to the mechanisms and kinetics of porphyroblast crystallisation. *Contributions to Mineralogy and Petrology*, **103**, 1–24.

Chouinard, A., Paquette, J. & Williams-Jones, A.E. 2005. Crystallographic controls on trace-element incorporation in auriferous pyrite from the Pascua epithermal high-sulfidation deposit, Chile-Argentina. *Canadian Mineralogist*, **43**, 951–963.

Ciobanu, C.L., Cook, N.J., Utsunomiya, S., Pring, A. & Green, L. 2011. Focussed ion beam–transmission electron microscopy applications in ore mineralogy: bridging micro- and nanoscale observations. *Ore Geology Reviews*, **42**, 6–31, https://doi.org/10.1016/j.oregeorev.2011.06.012

Cook, N.J., Ciobanu, C.L., Danyushevsky, L.V. & Gilbert, S. 2011. Minor and trace elements in bornite and associated Cu–(Fe)-sulfides: a LA-ICP-MS study. *Geochimica et Cosmochimica Acta*, **75**, 6473–6496, https://doi.org/10.1016/j.gca.2011.08.021

Cook, N.J., Ciobanu, C.L., Meria, D., Silcock, D. & Wade, B. 2013. Arsenopyrite-pyrite association in an orogenic gold ore: tracing mineralization history from textures and trace elements. *Economic Geology*, **108**, 1273–1283, https://doi.org/10.2113/econgeo.108.6.1273

Cox, S.F. 2010. The application of failure mode diagrams for exploring the roles of fluid pressure and stress states in controlling styles of fracture-controlled permeability enhancement in faults and shear zones. *Geofluids*, **10**, 217–233, https://doi.org/10.1111/j.1468-8123.2010.00281.x

Dare, S.A.S., Barnes, S.-J. & Prichard, H. 2010. The distribution of platinum group elements (PGE) and other chalcophile elements among sulfides from the Creighton Ni–Cu–PGE sulfide deposit, Sudbury, Canada, and the origin of palladium in pentlandite. *Mineralium Deposita*, **45**, 765–793, https://doi.org/10.1007/s00126-010-0295-6

Dare, S.A.S., Barnes, S.-J., Prichard, H.M. & Fisher, P.C. 2011. Chalcophile and platinum-group element (PGE) concentrations in the sulfide minerals from the McCreedy East deposit, Sudbury, Canada, and the origin of PGE in pyrite. *Mineralium Deposita*, **46**, 381–407.

Deditius, A.P., Utsunomiya, S., Reich, M., Kesler, S.E., Ewing, R.C., Hough, R. & Walshe, J. 2011. Trace metal nanoparticles in pyrite. *Ore Geology Reviews*, **42**, 32–46, https://doi.org/10.1016/j.oregeorev.2011.03.003

Demers, H., Gauvin, R., Brodusch, N. & Waters, K. 2013. Characterisation of rare earth minerals with

field emission scanning electron microscopy. *Canadian Metallurgical Quarterly*, **52**, 329–334, https://doi.org/10.1179/1879139513Y.0000000086

Duran, C.J., Barnes, S.-J. & Corkery, J.T. 2015. Chalcophile and platinum-group element distribution in pyrites from the sulfide-rich pods of the Lac des Iles Pd deposits, Western Ontario, Canada: implications for post-cumulus re-equilibration of the ore and the use of pyrite compositions in exploration. *Journal of Geochemical Exploration*, **158**, 223–242, https://doi.org/10.1016/j.gexplo.2015.08.002

Dyl, K.A., Cleverley, J.S., Bland, P.A., Ryan, C.G., Fisher, L.A. & Hough, R.M. 2014. Quantified, whole section trace element mapping of carbonaceous chondrites by synchrotron X-ray fluorescence microscopy: 1. CV meteorites. *Geochimica et Cosmochimica Acta*, **134**, 100–119, https://doi.org/10.1016/j.gca.2014.02.020

Etschmann, B., Ryan, C. *et al.* 2010. Reduced As components in highly oxidized environments: evidence from full spectral XANES imaging using the Maia massively parallel detector. *American Mineralogist*, **95**, 884–887, https://doi.org/10.2138/am.2010.3469

Etschmann, B., Brugger, J., Pearce, M.A., Ta, C., Brautigan, D., Jung, M. & Pring, A. 2014. Grain boundaries as microreactors during reactive fluid flow: experimental dolomitization of a calcite marble. *Contributions to Mineralogy and Petrology*, **168**, 1–12, https://doi.org/10.1007/s00410-014-1045-z

Evans, K.A., Phillips, G.N. & Powell, R. 2006. Rock-buffering of auriferous fluids in altered rocks associated with the Golden Mile-style mineralization, Kalgoorlie gold field, Western Australia. *Economic Geology*, **101**, 805.

Fisher, L.A. & Ryan, C.G. 2014. GeoPIXE element maps of sample GQ1943_3. *CSIRO Data Collection*, https://doi.org/10.4225/08/543DFA47E9878

Fisher, L.A., Cleverley, J.S., Pownceby, M. & MacRae, C. 2013. 3D representation of geochemical data, the corresponding alteration and associated REE mobility at the Ranger uranium deposit, Northern Territory, Australia. *Mineralium Deposita*, **48**, 947–966, https://doi.org/10.1007/s00126-013-0463-6

Fisher, L.A., Fougerouse, D. *et al.* 2015. Quantified, multi-scale X-ray fluorescence element mapping using the Maia detector array: application to mineral deposit studies. *Mineralium Deposita*, **50**, 665–674, https://doi.org/10.1007/s00126-014-0562-z

Fonteneau, L., Godel, B. & Ramanaidou, E. 2013. Application of high-resolution X-ray computed tomography to iron ore characterisation. *In*: *Proceedings Iron Ore 2013*. The Australasian Institute of Mining and Metallurgy, Melbourne, 243–250.

Fougerouse, D., Micklethwaite, S. *et al.* 2016*a*. Gold remobilisation and formation of high grade ore shoots driven by dissolution-reprecipitation replacement and Ni substitution into auriferous arsenopyrite. *Geochimica et Cosmochimica Acta*, **178**, 143–159.

Fougerouse, D., Reddy, S.M., Saxey, D.W., Rickard, W.D.A., Riessen, A. & Micklethwaite, S. 2016*b*. Nanoscale gold clusters in arsenopyrite controlled by growth rate not concentration: evidence from atom probe microscopy. *American Mineralogist*, **101**, 1916–1919, https://doi.org/10.2138/am-2016-5781CCBYNCND

Gadd, M., Layton-Matthews, D., Peter, J. & Paradis, S. 2015. The world-class Howard's Pass SEDEX Zn-Pb district, Selwyn Basin, Yukon. Part I: trace element compositions of pyrite record input of hydrothermal, diagenetic, and metamorphic fluids to mineralization. *Mineralium Deposita*, **50**, 1–24, https://doi.org/10.1007/s00126-015-0611-2

Gazley, M.F., Vry, J.K., du Plessis, E. & Handler, M.R. 2011. Application of portable X-ray fluorescence analyses to metabasalt stratigraphy, Plutonic Gold Mine, Western Australia. *Journal of Geochemical Exploration*, **110**, 74–80, https://doi.org/10.1016/j.gexplo.2011.03.002

Genna, D. & Gaboury, D. 2015. Deciphering the hydrothermal evolution of a VMS system by LA-ICP-MS using trace elements in pyrite: an example from the Bracemac-McLeod Deposits, Abitibi, Canada, and implications for exploration. *Economic Geology*, **110**, 2087–2108, https://doi.org/10.2113/econgeo.110.8.2087

Godel, B. 2013. High resolution X-ray computed tomography and its application to ore deposits: case studies from Ni-Cu-PGE deposits. *Economic Geology*, **108**, 2005–2019.

Godel, B. 2015. Platinum-group element deposits in layered intrusions: recent advances in the understanding of the ore forming processes. *In*: Charlier, B., Namur, O., Latypov, R. & Tegner, C. (eds) *Layered Intrusions*. Springer, Dordrecht, 379–432.

Godel, B. & Barnes, S.-J. 2008. Platinum-group elements in sulfide minerals and the whole rocks of the J-M Reef (Stillwater Complex): implication for the formation of the reef. *Chemical Geology*, **248**, 272–294.

Godel, B., Barnes, S.-J. & Maier, W.D. 2006. 3-D distribution of sulphide minerals in the Merensky Reef (Bushveld Complex, South Africa) and the J-M Reef (Stillwater Complex, USA) and their relationship to microstructures using X-ray computed tomography. *Journal of Petrology*, **47**, 1853–1872.

Godel, B., Barnes, S.-J. & Maier, W.D. 2007. Platinum-group elements in sulphide minerals, platinum-group minerals, and whole-rocks of the Merensky Reef (Bushveld Complex, South Africa): implications for the formation of the reef. *Journal of Petrology*, **48**, 1569–1604, https://doi.org/10.1093/petrology/egm030

Godel, B., Barnes, S.J., Barnes, S.-J. & Maier, W.D. 2010. Platinum ore in 3D: insights from high-resolution X-ray computed tomography. *Geology*, **38**, 1127–1130.

Godel, B., Barnes, S.J., Gürer, D., Austin, P. & Fiorentini, M.L. 2012*a*. Chromite in komatiites: 3D morphologies with implications for crystallization mechanisms. *Contributions to Mineralogy and Petrology*, **165**, 173–189, https://doi.org/10.1007/s00410-012-0804-y

Godel, B., Gonzalez-Alvarez, I., Barnes, S.J., Barnes, S.-J., Parker, P. & Day, J. 2012*b*. Sulfides and sulfarsenides from the Rosie Nickel Prospect, Duketon Greenstone Belt, Western Australia. *Economic Geology*, **107**, 275–294.

Godel, B., Barnes, S.J. & Barnes, S.-J. 2013. Deposition mechanisms of magmatic sulphide liquids: evidence

from high-resolution X-ray computed tomography and trace element chemistry of komatiite-hosted disseminated sulphides. *Journal of Petrology*, **54**, 1455–1481.

Godel, B., Rudashevsky, N.S., Nielsen, T.F.D., Barnes, S.J. & Rudashevsky, V.N. 2014. Constraints on the origin of the Skaergaard intrusion mineralization: insights from high-resolution X-ray computed tomography. *Lithos*, **190**, 27–36.

Gole, M.J. 2014. Leaching of S, Cu, and Fe from disseminated Ni-(Fe)-(Cu) sulphide ore during serpentinization of dunite host rocks at Mount Keith, Agnew-Wiluna belt, Western Australia. *Mineralium Deposita*, **49**, 821–842.

Gregory, M.J., Lang, J.R., Gilbert, S. & Hoal, K.O. 2013. Geometallurgy of the Pebble Porphyry copper-gold-molybdenum deposit, Alaska: implications for gold distribution and paragenesis. *Economic Geology*, **108**, 463–482, https://doi.org/10.2113/econgeo.108.3.463

Grguric, B.A., Rosengren, N.M., Fletcher, C.M. & Hronsky, J.M.A. 2006. Type 2 deposits: geology, mineralogy, and processing of the Mount Keith and Yakabindie orebodies, Western Australia. *In*: Barnes, S.J. (ed.) *Nickel Deposits of the Yilgarn Craton: Geology, Geochemistry, and Geophysics Applied to Exploration*. Society of Economic Geologists, Special Publications, **13**, 119–138.

Haest, M., Cudahy, T., Laukamp, C. & Gregory, S. 2012. Quantitative mineralogy from infrared spectroscopic data. II. Three-dimensional mineralogical characterization of the Rocklea channel iron deposit, Western Australia. *Economic Geology*, **107**, 229–249.

Hallberg, J.A. 1985. *Geology and Mineral Deposits of the Leonora-Laverton Area Northeastern Yilgarn Block, Western Australia*. Hesperian Press, Perth, Australia.

Hantler, A. 2009. *Paragenesis of mineralized veins at Sunrise Dam Gold Mine, Laverton, Western Australia*. MSc thesis, James Cook University.

Hill, E.J., Oliver, N.H.S., Cleverley, J.S., Nugus, M.J., Carswell, J. & Clark, F. 2014*a*. Characterisation and 3D modelling of a nuggety, vein-hosted gold ore body, Sunrise Dam, Western Australia. *Journal of Structural Geology*, **67** (Part B), 222–234, https://doi.org/10.1016/j.jsg.2013.10.013

Hill, E.J., Oliver, N.H.S., Fisher, L., Cleverley, J.S. & Nugus, M.J. 2014*b*. Using geochemical proxies to model nuggety gold deposits: an example from Sunrise Dam, Western Australia. *Journal of Geochemical Exploration*, **145**, 12–24, https://doi.org/10.1016/j.gexplo.2014.05.008

Hill, R.E.T. & Gole, M.J. 1990. Nickel sulfide deposits of the Yilgarn Block. *In*: Hughes, F.E. (ed.) *Geology of the Mineral Deposits of Australia and Papua New Guinea*. Parkville, Victoria, Australasian Institute of Mining and Metallurgy, Monograph, **14**, 557–559.

Hirth, G. & Tullis, J. 1994. The brittle-plastic transition in experimentally deformed quartz aggregates. *Journal of Geophysical Research*, **99**, 11731–11747.

Holwell, D.A. & McDonald, I. 2007. Distribution of platinum-group elements in the Platreef at Overysel, northern Bushveld Complex: a combined PGM and LA-ICP-MS study. *Contributions to Mineralogy and Petrology*, **154**, 171–190.

Holwell, D.A., Barnes, S.J., Le Vaillant, M., Keays, R.R., Fisher, L.A. & Prasser, R. 2016. 3D textural evidence for the formation of ultra-high tenor precious metal bearing sulphide microdroplets in offset reefs: an extreme example from the Platinova Reef, Skaergaard Intrusion, Greenland. *Lithos*, **256–257**, 55–74, https://doi.org/10.1016/j.lithos.2016.03.020

Hough, R.M., Noble, R.R.P. & Reich, M. 2011. Natural gold nanoparticles. *Ore Geology Reviews*, **42**, 55–61, https://doi.org/10.1016/j.oregeorev.2011.07.003

Hounsfield, G.N. 1973. Computerized transverse axial scanning (tomography).1. Description of system. *British Journal of Radiology*, **46**, 1016–1022.

Hronsky, J.M.A. & Schodde, R.C. 2006. Nickel exploration history of the Yilgarn Craton: from the nickel boom to today. *In*: Barnes, S.J. (ed.) *Nickel Deposits of the Yilgarn Craton: Geology, Geochemistry, and Geophysics Applied to Exploration*. Society of Economic Geologists, Special Publications, **13**, 1–11.

Hronsky, J.M.A., Groves, D.I., Loucks, R.R. & Begg, G.C. 2012. A unified model for gold mineralisation in accretionary orogens and implications for regional-scale exploration targeting methods. *Mineralium Deposita*, **47**, 339–358, https://doi.org/10.1007/s00126-012-0402-y

Huminicki, M.A.E., Sylvester, P.J., Cabri, L.J., Lesher, C.M. & Tubrett, M.N. 2005. Quantitative mass balance of platinum group elements in the Kelly Lake Ni-Cu-PGE deposit, Copper Cliff offset, Sudbury. *Economic Geology*, **100**, 1631–1646.

Jiang, Z., Prior, D.J. & Wheeler, J. 2000. Albite crystallographic preferred orientation and grain misorientation distribution in a low-grade mylonite; implications for granular flow. *Journal of Structural Geology*, **22**, 1663–1674.

Kenkmann, T. & Dresen, G. 2002. Dislocation microstructure and phase distribution in a lower crustal shear zone – an example from the Ivrea-Zone, Italy. *International Journal of Earth Sciences*, **91**, 445–458.

Kilburn, M.R. & Wacey, D. 2014. Nanoscale secondary ion mass spectrometry (NanoSIMS) as an analytical tool in the geosciences. *In*: Grice, K. (ed.) *Principles and Practice of Analytical Techniques in Geosciences*, The Royal Society of Chemistry, Cambridge, 1–34.

Kotula, P.G., Keenan, M.R. & Michael, J.R. 2003. Automated analysis of SEM X-ray spectral images: a powerful new microanalysis tool. *Microscopy and Microanalysis*, **9**, 1–17.

Kruse, R. & Stünitz, H. 1999. Deformation mechanisms and phase distribution in mafic high-temperature mylonites from the Jotun Nappe, southern Norway. *Tectonophysics*, **303**, 223–249.

Kyle, J.R. & Ketcham, R. 2003. In situ distribution of gold in ores using high-resolution X-ray computed tomography. *Economic Geology*, **98**, 1697–1701.

Kyle, J.R., Mote, A.S. & Ketcham, R. 2008. High resolution X-ray computed tomography studies of the Grasberg porphyry Cu-Au ores, Papua, Indonesia. *Mineralium Deposita*, **43**, 519–532.

Large, R.R., Maslennikov, V.V., Robert, F., Danyushevsky, L.V. & Chang, Z. 2007. Multistage sedimentary and metamorphic origin of pyrite and

gold in the Giant Sukhoi Log Deposit, Lena Gold Province, Russia. *Economic Geology*, **102**, 1233–1267, https://doi.org/10.2113/gsecongeo.102.7.1233

Large, R.R., Danyushevsky, L. *et al.* 2009. Gold and trace element zonation in pyrite using a laser imaging technique: implications for the timing of gold in orogenic and Carlin-style sediment-hosted deposits. *Economic Geology*, **104**, 635–668, https://doi.org/10.2113/gsecongeo.104.5.635

Lawley, C.J.M., Creaser, R.A. *et al.* 2015. Unraveling the Western Churchill Province Paleoproterozoic gold metallotect: constraints from Re-Os arsenopyrite and U-Pb xenotime geochronology and LA-ICP-MS arsenopyrite trace element chemistry at the BIF-hosted Meliadine Gold District, Nunavut, Canada. *Economic Geology*, **110**, 1425–1454, https://doi.org/10.2113/econgeo.110.6.1425

Leeman, W.P., Vicenzi, E., MacRae, C., Wilson, N., Torpy, A. & Lee, C.-T. 2008. Systematics of cathodoluminescence and trace element compositional zoning in natural quartz from volcanic rocks: Ti mapping in quartz. *Microscopy and Microanalysis*, **14**, 38–39, https://doi.org/10.1017/S1431927608088995

Leeman, W.P., MacRae, C.M. *et al.* 2012. A study of cathodoluminescence and trace element compositional zoning in natural quartz from volcanic rocks: mapping titanium content in quartz. *Microscopy and Microanalysis*, **18**, 1322–1341, https://doi.org/10.1017/S1431927612013426

Leiss, B. & Barber, D.J. 1999. Mechanisms of dynamic recrystallization in naturally deformed dolomite inferred from EBSP analyses. *Tectonophysics*, **303**, 51–69, https://doi.org/10.1016/S0040-1951(98)00258-3

Le Roux, S.G., Du Plessis, A. & Rozendaal, A. 2015. The quantitative analysis of tungsten ore using X-ray microCT: case study. *Computers & Geosciences*, **85** (Part A), 75–80, https://doi.org/10.1016/j.cageo.2015.09.009

Le Vaillant, M., Barnes, S., Fiorentini, M., Miller, J., McCuaig, T. & Muccilli, P. 2015. A hydrothermal Ni-As-PGE geochemical halo around the Miitel komatiite-hosted nickel sulfide deposit, Yilgarn Craton, Western Australia. *Economic Geology*, **110**, 505–530, https://doi.org/10.2113/econgeo.110.2.505

Le Vaillant, M., Barnes, S., Fiorentini, M., Santaguida, F. & Tormanen, T. 2016. Effects of hydrous alteration on the distribution of base metals and platinum group elements within the Kevitsa magmatic nickel sulphide deposit. *Ore Geology Reviews*, **72**, 128–148, https://doi.org/10.1016/j.oregeorev.2015.06.002

Li, K., Etschmann, B. *et al.* 2016. Ore petrography using megapixel X-ray imaging: rapid insights into element distribution and mobilization in complex Pt and U-Ge-Cu ores. *Economic Geology*, **111**, 487–501, https://doi.org/10.2113/econgeo.111.2.487

Liu, P.-P., Zhou, M.-F., Chen, W.T., Boone, M. & Cnudde, V. 2014. Using multiphase solid inclusions to constrain the origin of the Baima Fe–Ti–(V) oxide deposit, SW China. *Journal of Petrology*, **55**, 951–976, https://doi.org/10.1093/petrology/egu012

Lloyd, G.E. 1987. Atomic number and crystallographic contrast images with the SEM: a review of backscattered electron techniques. *Mineralogical Magazine*, **51**, 3–19.

MacRae, C.M., Wilson, N.C. & Brugger, J. 2009. Quantitative cathodoluminescence mapping with application to a Kalgoorlie scheelite. *Microscopy and Microanalysis*, **15**, 222–230, https://doi.org/10.1017/S1431927609090308

Maier, W., Rasmussen, B. *et al.* 2015. Petrogenesis of the similar to 2.77 Ga Monts de Cristal Complex, Gabon: evidence for direct precipitation of Pt-arsenides from basaltic magma. *Journal of Petrology*, **56**, 1285–1307, https://doi.org/10.1093/petrology/egv035

Mainprice, D. & Humbert, M. 1994. Methods of calculating petrophysical properties from lattice preferred orientation data. *Surveys in Geophysics*, **15**, 575–592, https://doi.org/10.1007/BF00690175

Mainprice, D., Bachmann, F., Hielscher, R., Schaeben, H. & Lloyd, G.E. 2014. Calculating anisotropic piezoelectric properties from texture data using the MTEX open source package. *In*: Faulkner, D.R., Mariani, E. & Mecklenburgh, J. (eds) *Rock Deformation from Field, Experiments and Theory: A Volume in Honour of Ernie Rutter*. Geological Society, London, Special Publications, **409**, 229–249, https://doi.org/10.1144/SP409.2

Mauger, A.J. & Hore, S. 2009. Integrating mineralogical interpretation of HyLogger data with HyMap Mineral Mapping, Mount Painter, South Australia. *In*: Jones, S. & Reinke, K. (eds) *Innovations in Remote Sensing and Photogrammetry*. Springer, Heidelberg, 271–280, https://doi.org/10.1007/978-3-540-93962-7_21

Mauger, A.J., Keeling, J.L. & Huntington, J.F. 2007. Alteration mapping of the Tarcoola Goldfield (South Australia) using a suite of hyperspectral methods. *Applied Earth Science*, **116**, 2–12, https://doi.org/10.1179/174327507X167028

McLellan, J.G., Blenkinsop, T., Nugus, M. & Erickson, M. 2007. Numerical simulations of deformation and controls on mineralization at the Sunrise Dam gold mine, Western Australia. *In*: Andrew, C.J. & Borg, G. (eds) *Digging Deeper, Proceedings of the Ninth Biennial SGA Meeting*, 20–23 August 2007, Dublin, Ireland, **2**, Irish Association for Economic Geology, Dublin, 1455–1458.

Meffre, S., Large, R.R. *et al.* 2015. Multi-stage enrichment processes for large gold-bearing ore deposits. *Ore Geology Reviews*, https://doi.org/10.1016/j.oregeorev.2015.09.002

Morales, L.F.G., Lagoeiro, L.E. & Endo, I. 2008. First results on the LPO-derived seismic properties of iron ores from the Quadrilatero Ferriffero region, southeastern Brazil. *Tectonophysics*, **460**, 21–33, https://doi.org/10.1016/j.tecto.2008.06.021

Muller, A., Wiedenbeck, M., Van den Kerkhof, A.M., Kronz, A. & Simon, K. 2003. Trace elements in quartz – a combined electron microprobe, secondary ion mass spectrometry, laser-ablation ICP-MS, and cathodoluminescence study. *European Journal of Mineralogy*, **15**, 747–763, https://doi.org/10.1127/0935-1221/2003/0015-0747

Mungall, J.E. 2002. Kinetic controls on the partitioning of trace elements between silicate and sulfide liquids. *Journal of Petrology*, **43**, 749–768.

Mungall, J.E. & Brenan, J.M. 2014. Partitioning of platinum-group elements and Au between sulfide liquid and basalt and the origins of mantle-crust fractionation of the chalcophile elements. *Geochimica et Cosmochimica Acta*, **125**, 265–289.

Newman, J. & Mitra, G. 1994. Fluid-influenced deformation and recrystallization of dolomite at low temperatures along a natural fault zone, Mountain City window, Tennessee. *Geological Society of America Bulletin*, **106**, 1267–1280, https://doi.org/10.1130/0016-7606(1994)106<1267:FIDARO>2.3.CO;2

Newton, P.G., Gibbs, D., Grove, A., Jones, C.M. & Ryall, A.W. 1998. Sunrise-Cleo gold deposit. *In*: Berkman, D.A. & Mackenzie, D.H. (eds) *Geology of Australian and Papua New Guinean Mineral Deposits*. The Australasian Institute of Mining and Metallurgy, Melbourne, 179–186.

Nugus, M., McCleod, T., Blenkinsop, T.G., Doyle, M. & Kent, M. 2005. Structural control of gold mineralization by reactivation of backthrusts at Sunrise Dam Gold Mine, Yilgarn craton, WA. *In*: Hancock, H., Fisher, L. *et al.* (eds) *Contributions of the Economic Geology Research Unit*, **64**, 188.

Nugus, M., Biggam, J., Clark, F. & Erickson, M. 2009. Development and application of macroscopic geological proxies for gold mineralisation in high nugget environments—an example from the Sunrise Dam Gold Mine, Western Australia. *Proceedings of the Seventh International Mining Geology Conference*. Melbourne, Australia, Australasian Institute of Mining and Metallurgy, 309–318.

Oliver, N.H.S., Nugus, M., Hill, E.J., Cleverley, J.S., Blenkinsop, T.G., Carswell, J. & Davidson, G. 2012. Vein-wallrock interaction and nuggety gold at Sunrise Dam, Western Australia. *Australian Institute of Geoscientists Bulletin*, **56**, 135–140.

Ord, A., Hobbs, B.E. & Lester, D.R. 2012. The mechanics of hydrothermal systems: i. Ore systems as chemical reactors. *Ore Geology Reviews*, **49**, 1–44, https://doi.org/10.1016/j.oregeorev.2012.08.003

Paterson, D., de Jonge, M.D. *et al.* 2011. The X-ray fluorescence microscopy beamline at the Australian synchrotron. *AIP Conference Proceedings*, **1365**, 219–222, https://doi.org/10.1063/1.3625343

Paul, B., Woodhead, J.D., Paton, C., Hergt, J.M., Hellstrom, J. & Norris, C.A. 2014. Towards a method for quantitative LA-ICP-MS imaging of multiphase assemblages: mineral identification and analysis correction procedures. *Geostandards and Geoanalytical Research*, **38**, 253–263, https://doi.org/10.1111/j.1751-908X.2014.00270.x

Pearce, M.A. 2015. EBSDinterp 1.0: a MATLAB® program to perform microstructurally constrained interpolation of EBSD data. *Microscopy and Microanalysis*, **21**, 985–993, https://doi.org/10.1017/S1431927615000781

Pearce, M.A. & Reddy, S.M. 2016. EBSD data from GQ - Sunrise Dam Goldmine, https://doi.org/10.4225/08/57C8FA3DA1653

Pearce, M.A., Timms, N.E., Hough, R.M. & Cleverley, J.S. 2013. Reaction mechanism for the replacement of calcite by dolomite and siderite: implications for geochemistry, microstructure and porosity evolution during hydrothermal mineralisation. *Contributions to Mineralogy and Petrology*, **166**, 995–1009, https://doi.org/10.1007/s00410-013-0905-2

Pearce, M.A., White, A.J.R., Fisher, L.A., Hough, R.M. & Cleverley, J.S. 2015. Gold deposition caused by carbonation of biotite during late-stage fluid flow. *Lithos*, **239**, 114–127, https://doi.org/10.1016/j.lithos.2015.10.010

Pearce, M.A., Fisher, L.A. & Ryan, C.G. 2016. Geo-PIXE element maps of samples GQ1943_2 and GQ1943_3. *CSIRO Data Collection*, https://doi.org/10.4225/08/57C8E0EE76B4E

Petrie, B., Craw, D. & Ryan, C. 2005. Geological controls on refractory ore in an orogenic gold deposit, Macraes mine, New Zealand. *Mineralium Deposita*, **40**, 45–58, https://doi.org/10.1007/s00126-005-0467-y

Piazolo, S., La Fontaine, A., Trimby, P., Harley, S., Yang, L., Armstrong, R. & Cairney, J.M. 2016. Deformation-induced trace element redistribution in zircon revealed using atom probe tomography. *Nature Communications*, **7**, 10490, https://doi.org/10.1038/ncomms10490

Pina, R., Gervilla, F., Barnes, S.-J., Ortega, L. & Lunar, R. 2012. Distribution of platinum-group and chalcophile elements in the Aguablanca Ni-Cu sulfide deposit (SW Spain): evidence from a LA-ICP-MS study. *Chemical Geology*, **302–303**, 61–75.

Prichard, H.M., Barnes, S.J. *et al.* 2015. The structure of and origin of nodular chromite from the Troodos ophiolite, Cyprus, revealed using high-resolution X-ray computed tomography and electron backscatter diffraction. *Lithos*, **218–219**, 87–98, https://doi.org/10.1016/j.lithos.2015.01.013

Prior, D.J., Boyle, A.P. *et al.* 1999. The application of electron backscatter diffraction and orientation contrast imaging in the SEM to textural problems in rocks. *American Mineralogist*, **84**, 1741–1759.

Prior, D.J., Mariani, E. & Wheeler, J. 2009. EBSD in the earth sciences: applications, common practice and challenges. *In*: Schwatz, A.J., Kumar, M., Adams, B.L. & Field, D.P. (eds) *Electron Backscatter Diffraction in Materials Science*. Springer, New York.

Putnis, A. 2009. Mineral replacement reactions. *Reviews in Mineralogy and Geochemistry*, **70**, 87–124, https://doi.org/10.2138/rmg.2009.70.3

Qian, G., Brugger, J., Skinner, W.M., Chen, G. & Pring, A. 2010. An experimental study of the mechanism of the replacement of magnetite by pyrite up to 300 degrees C. *Geochimica et Cosmochimica Acta*, **74**, 5610–5630, https://doi.org/10.1016/j.gca.2010.06.035

Reddy, S.M. & Hough, R.M. 2013. Microstructural evolution and trace element mobility in Witwatersrand pyrite. *Contributions to Mineralogy and Petrology*, **166**, 1269–1284, https://doi.org/10.1007/s00410-013-0925-y

Reich, M., Utsunomiya, S., Kesler, S.E., Wang, L., Ewing, R.C. & Becker, U. 2006. Thermal behavior of metal nanoparticles in geologic materials. *Geology*, **34**, 1033–1036, https://doi.org/10.1130/G22829A.1

Ritchie, N.W.M., Newbury, D.E. & Davis, J.M. 2012. EDS measurements of X-ray intensity at WDS precision and accuracy using a silicon drift detector.

Microscopy and Microanalysis, **18**, 892–904, https://doi.org/10.1017/S1431927612001109

Roache, T.J., Walshe, J.L. *et al.* 2011. Epidote-clinozoisite as a hyperspectral tool in exploration for Archean gold. *Australian Journal of Earth Sciences*, **58**, 813–822, https://doi.org/10.1080/08120099.2011.608170

Robertson, J.C., Barnes, S.J. & Le Vaillant, M. 2015. Dynamics of magmatic sulphide droplets during transport in silicate melts and implications for magmatic sulphide ore formation. *Journal of Petrology*, **56**, 2445–2472, https://doi.org/10.1093/petrology/egv078

Rosengren, N.M., Beresford, S.W., Grguric, B.A. & Cas, R.A.F. 2005. An intrusive origin for the komatiitic dunite-hosted Mount Keith disseminated nickel sulfide deposit, Western Australia. *Economic Geology*, **100**, 149–156.

Rosengren, N.M., Cas, R.A.F., Beresford, S.W. & Palich, B.M. 2008. Reconstruction of an extensive Archean dacitic submarine volcanic complex associated with komatiite-hosted Mt Keith nickel deposit, Agnew-Wiluna Greenstone Belt, Yilgarn Craton, Western Australia. *Precambrian Research*, **161**, 34–52.

Rosiere, C.A., Garcia, O.L., Siemes, H. & Schaeben, H. 2013. Domainal fabrics of hematite in schistose, shear zone-hosted high-grade Fe ores: the product of the interplay between deformation and mineralization. *Journal of Structural Geology*, **55**, 150–166, https://doi.org/10.1016/j.jsg.2013.07.017

Rusk, B. & Reed, M. 2002. Scanning electron microscope-cathodoluminescence analysis of quartz reveals complex growth histories in veins from the Butte porphyry copper deposit, Montana. *Geology*, **30**, 727–730, https://doi.org/10.1130/0091-7613 (2002)030<0727:SEMCAO>2.0.CO;2

Rusk, B., Koenig, A. & Lowers, H. 2011. Visualizing trace element distribution in quartz using cathodoluminescence, electron microprobe, and laser ablation-inductively coupled plasma-mass spectrometry. *American Mineralogist*, **96**, 703–708, https://doi.org/10.2138/am.2011.3701

Ryan, C.G. 2000. Quantitative trace element imaging using PIXE and the nuclear microprobe. *International Journal of Imaging Systems and Technology*, **11**, 219–230, https://doi.org/10.1002/ima.1007

Ryan, C.G. 2001. Developments in dynamic analysis for quantitative PIXE true elemental imaging. *Nuclear Instruments and Methods in Physics Research Section B: Beam Interactions with Materials and Atoms*, **181**, 170–179, https://doi.org/10.1016/S0168-583X(01)00374-3

Ryan, C.G., Jamieson, D.N., Churms, C.L. & Pilcher, J.V. 1995. A new method for online true-element imaging using PIXE and the proton microprobe. *Nuclear Instruments and Methods in Physics Research Section B: Beam Interactions with Materials and Atoms*, **104**, 157–165, https://doi.org/10.1016/0168-583X(95)00404-1

Ryan, C.G., van Achterbergh, E., Yeats, C.J., Tin Win, T. & Cripps, G. 2002. Quantitative PIXE trace element imaging of minerals using the new CSIRO–GEMOC nuclear microprobe. *Nuclear Instruments and Methods in Physics Research Section B: Beam Interactions with Materials and Atoms*, **189**, 400–407, https://doi.org/10.1016/S0168-583X(01)01098-9

Ryan, C.G., Van Achterbergh, E. & Jamieson, D.N. 2005. Advances in dynamic analysis PIXE imaging: correction for spatial variation of pile-up components. *Nuclear Instruments and Methods in Physics Research Section B: Beam Interactions with Materials and Atoms*, **231**, 162–169.

Ryan, C.G., Siddons, D.P. *et al.* 2014. Maia X-ray fluorescence imaging: capturing detail in complex natural samples. *Journal of Physics Conference Series*, **499**, https://doi.org/10.1088/1742-6596/499/1/012002

Ryan, C.G., Laird, J.S., Fisher, L.A., Kirkham, R. & Moorhead, G.F. 2015. Improved dynamic analysis method for quantitative PIXE and SXRF element imaging of complex materials. *Nuclear Instruments and Methods in Physics Research Section B: Beam Interactions with Materials and Atoms*, **363**, 42–47, https://doi.org/10.1016/j.nimb.2015.08.021

Schumann, D., Fuchs, S. *et al.* 2014. Combining terapixel-scale SEM imaging and high-resolution TEM studies for mineral exploration. *Microscopy and Microanalysis*, **20**, 1008–1009, https://doi.org/10.1017/S143192761400676X

Shore, M. & Fowler, A.D. 1996. Oscillatory zoning in minerals: a common phenomenon. *Canadian Mineralogist*, **34**, 1111–1126.

Sibson, R.H., Robert, F. & Poulsen, K.H. 1988. High-angle reverse faults, fluid-pressure cycling, and mesothermal gold-quartz deposits. *Geology*, **16**, 551–555, https://doi.org/10.1130/0091-7613(1988)016<0551:HARFFP>2.3.CO;2

Simon, G., Kesler, S.E. & Chryssoulis, S. 1999. Geochemistry and textures of gold-bearing arsenian pyrite, Twin Creeks, Nevada; implications for deposition of gold in Carlin-type deposits. *Economic Geology*, **94**, 405–421, https://doi.org/10.2113/gsecongeo.94.3.405

Steele, I.M., Cabri, L.J., Gaspar, J.C., McMahon, G., Marquez, M.A. & Vasconcellos, M.A.Z. 2000. Comparative analysis of sulfides for gold using SXRF and SIMS. *The Canadian Mineralogist*, **38**, 1–10, https://doi.org/10.2113/gscanmin.38.1.1

Sung, Y.-H., Brugger, J., Ciobanu, C.L., Pring, A., Skinner, W. & Nugus, M. 2009. Invisible gold in arsenian pyrite and arsenopyrite from a multistage Archaean gold deposit: Sunrise Dam, Eastern Goldfields Province, Western Australia. *Mineralium Deposita*, **44**, 765–791, https://doi.org/10.1007/s00126-009-0244-4

Thomas, H.V., Large, R.R. *et al.* 2011. Pyrite and pyrrhotite textures and composition in sediments, laminated quartz veins, and reefs at Bendigo Gold Mine, Australia: insights for ore genesis. *Economic Geology*, **106**, 1–31, https://doi.org/10.2113/econgeo.106.1.1

Trimby, P.W. 2012. Orientation mapping of nanostructured materials using transmission Kikuchi diffraction in the scanning electron microscope. *Ultramicroscopy*, **120**, 16–24, https://doi.org/10.1016/j.ultramic.2012.06.004

Valley, J.W., Cavosie, A.J. *et al.* 2014. Hadean age for a post-magma-ocean zircon confirmed by atom-probe tomography. *Nature Geoscience*, **7**, 219–223, https://doi.org/10.1038/ngeo2075

Vasyukova, O.V., Goemann, K., Kamenetsky, V.S., MacRae, C.M. & Wilson, N.C. 2013. Cathodoluminescence properties of quartz eyes from porphyry-type deposits: implications for the origin of quartz. *American Mineralogist*, **98**, 98–109, https://doi.org/10.2138/am.2013.4018

Vukmanovic, Z., Barnes, S.J., Reddy, S.M., Godel, B. & Fiorentini, M.L. 2012. Morphology and microstructure of chromite crystals in chromitites from the Merensky Reef (Bushveld Complex, South Africa). *Contributions to Mineralogy and Petrology*, **165**, 1031–1050, https://doi.org/10.1007/s00410-012-0846-1

Vukmanovic, Z., Reddy, S.M., Godel, B., Barnes, S.J., Fiorentini, M.L., Barnes, S.-J. & Kilburn, M.R. 2014. Relationship between microstructures and grain-scale trace element distribution in komatiite-hosted magmatic sulphide ores. *Lithos*, **184**, 42–61, https://doi.org/10.1016/j.lithos.2013.10.037

Wark, D.A. & Watson, E.B. 2006. TitaniQ: a titanium-in-quartz geothermometer. *Contributions to Mineralogy and Petrology*, **152**, 743–754, https://doi.org/10.1007/s00410-006-0132-1

Warren, M.R., Hanley, J.J., Ames, D.E. & Jackson, S.E. 2015. The Ni–Cr–Cu content of biotite as pathfinder elements for magmatic sulfide exploration associated with mafic units of the Sudbury Igneous Complex, Ontario, Canada. *Journal of Geochemical Exploration*, **153**, 11–29, https://doi.org/10.1016/j.gexplo.2015.02.010

Watt, G.R., Griffin, B.J. & Kinny, P.D. 2000. Charge contrast imaging of geological materials in the environmental scanning electron microscope. *American Mineralogist*, **85**, 1784–1794, https://doi.org/10.2138/am-2000-11-1221

Wheeler, J. 2014. Dramatic effects of stress on metamorphic reactions. *Geology*, **42**, 647–650, https://doi.org/10.1130/G35718.1

White, A.J.R., Smith, R.E., Nadoll, P. & Legras, M. 2014. Regional-scale metasomatism in the Fortescue Group Volcanics, Hamersley Basin, Western Australia: implications for hydrothermal ore systems. *Journal of Petrology*, **55**, 977–1009, https://doi.org/10.1093/petrology/egu013

Wilson, N.C. & MacRae, C.M. 2005. An automated hybrid clustering technique applied to spectral data sets. *Microscopy and Microanalysis*, **11**, 434–435, https://doi.org/10.1017/S1431927605501168

Xia, F., Brugger, J., Chen, G., Ngothai, Y., O'Neill, B., Putnis, A. & Pring, A. 2009. Mechanism and kinetics of pseudomorphic mineral replacement reactions: a case study of the replacement of pentlandite by violarite. *Geochimica et Cosmochimica Acta*, **73**, 1945–1969, https://doi.org/10.1016/j.gca.2009.01.007

Xie, Y., Li, Y. *et al.* 2009. Magmatic evolution and characteristics of magmatic fluid in the Qiagong porphyry system. *Acta Geologica Sinica*, **83**, 1869–1886.

Yeats, C., Belton, D., Laird, J.S. & Ryan, C.G. 2010. Mapping elemental distributions in submarine hydrothermal sulfide smokers using proton induced X-ray emission. *Nuclear Instruments and Methods in Physics Research Section B: Beam Interactions with Materials and Atoms*, **268**, 2129–2132, https://doi.org/10.1016/j.nimb.2010.02.034

Yuan, Z., Cheng, Q., Xia, Q., Yao, L., Chen, Z., Zuo, R. & Xu, D. 2014. Spatial patterns of geochemical elements measured on rock surfaces by portable X-ray fluorescence: application to hand specimens and rock outcrops. *Geochemistry: Exploration, Environment, Analysis*, **14**, 265–276, https://doi.org/10.1144/geochem2012-173

Zhang, J., Lin, Y., Yang, W., Shen, W., Hao, J., Hu, S. & Cao, M. 2014*a*. Improved precision and spatial resolution of sulfur isotope analysis using NanoSIMS. *Journal of Analytical Atomic Spectrometry*, **29**, 1934–1943, https://doi.org/10.1039/C4JA00140K

Zhang, J., Deng, J., Chen, H., Yang, L., Cooke, D., Danyushevsky, L. & Gong, Q. 2014*b*. LA-ICP-MS trace element analysis of pyrite from the Chang'an gold deposit, Sanjiang region, China: implication for ore-forming process. *Gondwana Research*, **26**, 557–575, https://doi.org/10.1016/j.gr.2013.11.003

Zhao, J., Brugger, J., Grundler, P.V., Xia, F., Chen, G. & Pring, A. 2009. Mechanism and kinetics of a mineral transformation under hydrothermal conditions: calaverite to metallic gold. *American Mineralogist*, **94**, 1541–1555, https://doi.org/10.2138/am.2009.3252

Zhao, X.-F., Zhou, M.-F., Hitzman, M.W., Li, J.-W., Bennett, M., Meighan, C. & Anderson, E. 2012. Late Paleoproterozoic to Early Mesoproterozoic Tangdan sedimentary rock-hosted strata-bound copper deposit, Yunnan Province, southwest China. *Economic Geology*, **107**, 357–375, https://doi.org/10.2113/econgeo.107.2.357